

Computation of Free Energy Profile at ab initio QM/MM Level Made Orders of Magnitude Faster via the Reference-Potential Approach Using Weighted Thermodynamics Perturbation

Pengfei Li,[†] Xiangyu Jia,^{†,§} Yihan Shao,[‡] and Ye Mei^{*,†,¶,‡}

[†]*State Key Laboratory of Precision Spectroscopy, School of Physics and Materials Science,
East China Normal University, Shanghai 200062, China*

[‡]*Department of Chemistry and Biochemistry, University of Oklahoma, Norman OK 73019,
United States of America*

[¶]*NYU-ECNU Center for Computational Chemistry at NYU Shanghai, Shanghai 200062,
China*

[§]*Current address: NYU-ECNU Center for Computational Chemistry at NYU Shanghai,
Shanghai 200062, China*

E-mail: ymei@phy.ecnu.edu.cn

Abstract

Free energy profile (FE Profile) is an essential quantity for the estimation of reaction rate and the validation of reaction mechanism. For chemical reactions in condensed phase or enzymatic reactions, the computation of FE profile at *ab initio* (*ai*) quantum mechanical/molecular mechanics (QM/MM) level is still far too expensive. Semiempirical (SE) method can be hundreds or thousands of times faster than the *ai* methods. However, the accuracy of SE methods is often unsatisfactory, due to the approximations that have been adopted in these methods. In this work, we proposed a new method termed MBAR+wTP, in which the *ai* QM/MM free energy profile is computed by a weighted thermodynamic perturbation (TP) correction to the SE profile generated by the multistate Bennett acceptance ratio (MBAR) analysis of the trajectories from umbrella samplings (US). The weight factors used in the TP calculations are a byproduct of the MBAR analysis in the post-processing of the US trajectories, which are often discarded after the free energy calculations. The results show that this approach can enhance the efficiency of *ai* FE profile calculations by several orders of magnitude.

1 Introduction

Free energy profile (FE profile), defined as the free energy variation along the reaction coordinate(s) (RC), is now widely used to calculate the reaction rate and to examine the reaction mechanism.¹ Based on the transition state theory (TST), the reaction rate is determined by the free energy barrier and the curvature of the free energy profile near the transition state.^{2,3} Due to the exponential decrease of the population with respect to the free energy, a brutal force simulation is always insufficient for the states away from the reactant and the product. Umbrella sampling (US) is now routinely employed to enhance the sampling of the system along the RC by restraining the RC around a series of values using biasing potentials. The trajectories are then analyzed using the multistate Bennett acceptance ratio (MBAR)^{4,5} or its binned variant the weighted histogram analysis method (WHAM)⁶⁻⁹ to construct the free energy profile. Multiple windows are required in the US sampling, and the number of windows is determined by the curvature of the free energy profile. MBAR and WHAM are global algorithms, which assume that a global equilibrium of all the windows have been reached.¹⁰ Besides, the samples must be as statistically independent as possible. In order to obtain a statistically sound result, a long time simulation for each window is needed.

For the studies of chemical reactions in condensed phase, classical force fields, which lack a finite bond-dissociation energy, are in general not applicable. On the other end of the methodological spectrum, full quantum mechanical methods are not feasible either due to the extremely poor computational scaling with the system size. The hybrid quantum mechanical/molecular mechanical method (QM/MM)¹¹ inherits the advantages from both sides, which makes it an appealing method and is nowadays routinely employed. However, the convergence of the FE profiles for chemical and enzymatic reactions in condensed phase is very slow, which requires exhaustive sampling in the high-dimensional phase space, and makes the computation of the FE profile at the *ab initio* (*ai*) QM/MM levels¹²⁻¹⁴ notoriously time consuming, if feasible at all. Therefore, a great amount of QM/MM simulations

employed semiempirical (SE) methods such as PM3,¹⁵ AM1,¹⁶ MNDO,¹⁷ PM6,¹⁸ empirical valence bond (EVB),^{19–21} and density functional theory-based tight-binding (DFTB)^{22,23} as well as its self-consistent-charge variant (SCC-DFTB).²⁴ Nevertheless, the results from QM/MM simulations employing an SE Hamiltonian are often of poor accuracy in terms of the reaction free energy and free energy barrier.²⁵ Consequently, developing an efficient method for the computation of state free energy and free energy profile at *ai* QM/MM level remains one of the major challenges in modern computational chemistry.

In a pioneer work, Gao applied the dual-Hamiltonian method, aka the reference-potential method, in a study of the hydration free energy.^{26,27} Warshel et al. proposed another dual-Hamiltonian approach to calculate the FE profile for a chemical reaction,²⁸ which was later named the paradynamics (PD) method.^{29–31} In this method, an initial simulation is carried out utilizing EVB as a reference-potential, which is reasonably close to the real potential, allowing one to use a perturbation rectification in the subsequent step to obtain the free energy profile at the *ai* level. However, constructing the EVB potential energy surface is nontrivial. Rod and Ryde computed the free energy barrier for a methyl transfer reaction catalyzed by the enzyme catechol O-methyltransferase using a dual Hamiltonian approach, in which the free energy profile sampled at a molecular mechanical level was corrected to the level of density functional theory using thermodynamic perturbation.³² However, in their study, the QM degrees-of-freedom were not sampled, which inevitably led to overestimation of the free energy. Beierlein et al applied this idea in the calculation of free energy in protein-ligand association.³³ Polyak et al designed a dual Hamiltonian free energy perturbation (DH-FEP) method to calculate the free energy profiles of a model system and chorismate mutase.³⁴ However, their method was not rigorous, because in the TP calculation the configurations were sampled on a low-level Hamiltonian but the energy difference between two windows were calculated on a high-level Hamiltonian. In addition, the constrained dynamics always overestimates the free energy difference in TP calculations. More importantly, the configurations of the target RC were not unambiguous when taken into the TP calculations. Therefore, the

calculation with two-dimensional RCs worked better than the one with a one-dimensional RC. König combined energy reweighting with Bennett acceptance ratio and developed a new method called non-Boltzmann Bennett acceptance ratio (NBB). However, this method does not yield a minimum variance for the results.^{35,36} Hudson et al incorporated energy reweighting into the chain-of-replicas method for the computation of pathway free energy.³⁷ Because the chain-of-replicas method is a global simulation method instead of a pure post-processing method, the implementation of the reweighting is not trivial. Hudson et al also used the non-equilibrium simulation method to correct the free energy profile of a low-level Hamiltonian to a high-level one.³⁸ However, this method requires expensive energy/force evaluation on the high-level Hamiltonian for every step of the simulation, which is not the preferred method in the first place for such studies.³⁹

In our previous work,⁴⁰ the dual-Hamiltonian approach was used to calculate the solvation free energies of the molecules in the SAMPL4 via an alchemical decoupling process. A classical force field was chosen as the reference-potential, on which level the solvation free energies were estimated using BAR or its multistate variant MBAR. Then a direct TP calculation was performed to obtain the MM-to-QM/MM correction. It has been shown that this (M)BAR+TP method yielded minimum variance for the free energy. Since this (M)BAR+TP method can be applied in the calculation of free energy difference between two thermodynamic states, quite naturally it can also be applied to the calculation of FE profile, because free energy difference between two thermodynamic states is calculated as a generalized FE profile in an extended phase space with one dimension of the coupling parameter appended to the normal phase space. Dybeck incorporated the dual Hamiltonian method with MBAR in the calculation of free energy difference between two states, which can be put forward to the calculations of FE profile.⁴¹ Although this method yields the globally minimal variance for the free energies, it is a $O(N^2)$ algorithm, where N is the number of the intermediate states.

Another class of approaches that has become a new boost in computational chemistry

is machine learning (ML) or deep learning (DL).^{42,43} Based on some training using neural network, an energy correction term in a high-dimensional space (probably a complete phase space or a subspace of it) can be learned. Consequently, potential energy and/or force on the high-level Hamiltonian can be accurately estimated for the structural ensemble generated at the low-level Hamiltonian.^{44–51} However, for most cases the learned energy/force correction for a chemical reaction is system-specific short of transferability to other reactions, and the training itself is expensive. Even before the introduction of ML into this field, parameter tuning to the high-level *ai* accuracy for the SE methods and force fields to conduct the simulation have been performed by many groups.^{52–58}

In this work, we applied MBAR+TP to the calculations of the FE profiles of one quasi-chemical reaction and three chemical reactions in aqueous solution as shown in Fig. 1, including (a) main chain dihedral rotation of a butane molecule, (b) S_N2 reaction of $\text{CH}_3\text{Cl} + \text{Cl}^- \longrightarrow \text{Cl}^- + \text{CH}_3\text{Cl}$, (c) Glycine intramolecular proton transfer reaction from the neutral form to the zwitterion form, and (d) aliphatic Claisen rearrangement reaction of allyl vinyl ether (AVE) to 4-pentenal. We show that the FE profile of high-level Hamiltonian can be obtained in this way with configuration sampling carried out only using the low-level Hamiltonian, and only one hundredth of the configurations were used for the high-level energy calculations. As a consequence, the formidably expensive sampling using the high-level Hamiltonian is avoided, thus enhancing the efficiency by several orders of magnitude.

2 Method

2.1 Umbrella Sampling and Multistate Bennett Acceptance Ratio

For reactions in condensed phase, the reactant and the product states are often separated by a free energy barrier, hindering the transition between these two states. In order to characterize this free energy barrier, a reaction path defined by reaction coordinates (RC) $\eta(\mathbf{x})$ in a low dimension should be carefully chosen, and the free energy profile along the reaction path

from the reactant to the product is proportional to the logarithm of the probability of visit by the system. The reaction coordinate $\eta(\mathbf{x})$ is usually a function of the collective atomic coordinates \mathbf{x} . The reaction rate can be estimated by the ratio of the free energy barrier over $k_B T$, where k_B is Boltzmann constant and T is the temperature. When the reaction barrier is much greater than $k_B T$, which is often the case for chemical reactions under mild conditions, the probability of visit to the regions away from either the reactant or the product is rare, especially the visit to the transition state, and computational cost for the brutal force simulation is far beyond what we can afford with modern computers. Umbrella sampling (US) method⁵⁹ is a solution to this situation, and it is routinely used nowadays. US is a stratified approach, and each stratum samples a limited range of phase space along the RC by augmenting the original potential energy surface $U_0(\mathbf{x})$ with a restraining bias $W_i(\eta)$. A harmonic potential is frequently used as the bias $W_i(\eta) = \frac{1}{2}k_i(\eta - \eta_i)^2$, where η_i and k_i are the target value of RC and the strength of the restraint, respectively, for the i th biased window. The trajectories from a set of biased window simulations indexed by i ($i = 1, 2, \dots, S$) with the potential energy surfaces $U_i^{(b)}(\eta) = U_0(\mathbf{x}) + W_i(\eta(\mathbf{x}))$ are then post-processed using the Weighted Histogram Analysis Method (WHAM)⁶⁻⁹ or its “binless” variant the Multistate Bennett Acceptance Ratio (MBAR)^{4,5} globally to obtain the unbiased thermodynamic properties on the original potential energy surface U_0 . Both methods have been well-documented in the literature.⁴⁻⁹ Here, we will present a brief explanation of the MBAR method for the analysis of US simulations.

According to the MBAR method,^{4,5} the free energy $f_t^{(b)}$ of the t th biased simulation

window can be obtained by

$$\begin{aligned}
e^{-\beta f_t^{(b)}} &= \sum_{i=1}^S \sum_{l=1}^{N_i} \frac{e^{-\beta U_t^{(b)}(\mathbf{x}_{i,l})}}{\sum_{k=1}^S N_k e^{-\beta [U_k^{(b)}(\mathbf{x}_{i,l}) - f_k^{(b)}]}} \\
&= \sum_{i=1}^S \sum_{l=1}^{N_i} \frac{e^{-\beta [U_0(\mathbf{x}_{i,l}) + W_t(\mathbf{x}_{i,l})]}}{\sum_{k=1}^S N_k e^{-\beta [U_0(\mathbf{x}_{i,l}) + W_k(\mathbf{x}_{i,l}) - f_k^{(b)}]}} \\
&= \sum_{i=1}^S \sum_{l=1}^{N_i} \frac{e^{-\beta [W_t(\mathbf{x}_{i,l})]}}{\sum_{k=1}^S N_k e^{-\beta [W_k(\mathbf{x}_{i,l}) - f_k^{(b)}]}}, \tag{1}
\end{aligned}$$

where $\mathbf{x}_{i,l}$ is the l th frame among N_i configurations in the i th biased simulation. Since $f_t^{(b)}$ appear on both the left-hand side and the right-hand side of Eq. 1, they should be solved iteratively. Sorting the samples into bins are unnecessary. In other words, MBAR is equivalent to WHAM in the limit that bin widths shrunk to zero and can be derived without the need to invoke histograms.⁴ It is worth emphasizing that $f_t^{(b)}$ is unnecessarily among $\{f_k^{(b)}, k = 1, \dots, K\}$. It can be the free energy of any state of the system with a potential energy function $U_t(\mathbf{x}) = U_0(\mathbf{x}) + W_t(\mathbf{x})$. If $W_t(\mathbf{x}) = 0$, $U_t(\mathbf{x})$ equals to the unbiased potential energy $U_0(\mathbf{x})$, and $f_t^{(b)}$ becomes the unbiased free energy f_0 .

The weight of the l th configuration in the i th biased simulation for any Hamiltonian U_t is, akin to Eq. 9 in ref. 4,

$$w_t(\mathbf{x}_{i,l}) = \frac{e^{-\beta [U_t(\mathbf{x}_{i,l}) - f_t]}}{\sum_{k=1}^S N_k e^{-\beta [U_k^{(b)}(\mathbf{x}_{i,l}) - f_k^{(b)}]}}. \tag{2}$$

This definition ensures that $\sum_{i=1}^S \sum_{l=1}^{N_i} w_t(\mathbf{x}_{i,l}) = 1$ for all $t = 1, 2, \dots, S$ and $\sum_{t=1}^S N_t w_t(\mathbf{x}_{i,l}) = 1$ for all $\mathbf{x}_{i,l}$, where $i = 1, 2, \dots, S; l = 1, 2, \dots, N_i$. The unbiased probability $\rho_0(\eta)$ can be

calculated now by

$$\rho_0(\eta) = \sum_{i=1}^S \sum_{l=1}^{N_i} \frac{\delta(\mathbf{x}_{\eta(i,l)} - \mathbf{x}_{i,l})}{\sum_{k=1}^S N_k e^{-\beta[W_k(\mathbf{x}_{i,l}) - f_k^{(b)}]}}, \quad (3)$$

and the free energy profile is calculated as

$$\begin{aligned} F(\eta) &= -\beta^{-1} \ln \rho_0(\eta) \\ &= -\beta^{-1} \ln \sum_{i=1}^S \sum_{l=1}^{N_i} \frac{\delta(\mathbf{x}_{\eta(i,l)} - \mathbf{x}_{i,l})}{\sum_{k=1}^S N_k e^{-\beta[W_k(\mathbf{x}_{i,l}) - f_k^{(b)}]}}. \end{aligned} \quad (4)$$

The covariance matrix can be obtained from Eq. D8 in Ref. 4 by

$$\boldsymbol{\Theta} = \left[(\mathbf{W}^T \mathbf{W})^{-1} - \mathbf{N} + \mathbf{1}_{S+M} \mathbf{1}_{S+M}^T / N \right]^{-1}, \quad (5)$$

where \mathbf{N} is a $(S+M) \times (S+M)$ matrix, $\mathbf{N} = \text{diag}(N_1, N_2, \dots, N_S, 0_1, 0_2, \dots, 0_M)$, M denotes the number of histogram bins and $N = \sum_{i=1}^S \sum_{l=1}^{N_i} 1$ is the total number of samples collected from all the biased simulations, and \mathbf{W} is the weight matrix with a dimension of $N \times (S+M)$.

The $N \times S$ elements of \mathbf{W} can be obtained via

$$w_i(\mathbf{x}_{i,l}) = \frac{e^{-\beta[W_i(\mathbf{x}_{i,l}) - f_i^{(b)}]}}{\sum_{k=1}^S N_k e^{-\beta[W_k(\mathbf{x}_{i,l}) - f_k^{(b)}]}}. \quad (6)$$

The $N \times M$ elements of \mathbf{W} can be obtained by

$$w_\eta(\mathbf{x}_{i,l}) = \frac{\frac{\delta(\mathbf{x}_{\eta(i,l)} - \mathbf{x}_{i,l})}{\sum_{k=1}^S N_k e^{-\beta[W_k(\mathbf{x}_{i,l}) - f_k^{(b)}]}}}{\sum_{i=1}^S \sum_{l=1}^{N_i} \frac{\delta(\mathbf{x}_{\eta(i,l)} - \mathbf{x}_{i,l})}{\sum_{k=1}^S N_k e^{-\beta[W_k(\mathbf{x}_{i,l}) - f_k^{(b)}]}}}. \quad (7)$$

The uncertainty in the estimated free energy difference can be computed as

$$\delta^2 \Delta F(\eta_{ij}) = \Theta_{ii} - 2\Theta_{ij} + \Theta_{jj}. \quad (8)$$

2.2 Weighted Thermodynamic Perturbation

Thermodynamic Perturbation (TP), also known as Free Energy Perturbation, exponential average, and Zwanzig equation was developed by Zwanzig.⁶⁰ In TP, only one simulation (normally with the inexpensive Hamiltonian) is required and the free energy difference between the target Hamiltonian and the sampled Hamiltonian can be calculated with the sampled configurations. Using the binned configurations from the US simulations and their weights from the MBAR analysis, the FE profile at high level Hamiltonian can be calculated by TP. According to Eq. 2, the weight for the l th configuration in the i th biased simulation under the low-level Hamiltonian, which is the unbiased SE Hamiltonian in this study, is

$$\begin{aligned} w_L(\mathbf{x}_{i,l}) &= \frac{e^{-\beta[U_L(\mathbf{x}_{i,l}) - f_L]}}{\sum_{k=1}^S N_k e^{-\beta[U_k^{(b)}(\mathbf{x}_{i,l}) - f_k^{(b)}]}} \\ &= \frac{e^{\beta f_L}}{\sum_{k=1}^S N_k e^{-\beta[W_k(\mathbf{x}_{i,l}) - f_k^{(b)}]}}, \end{aligned} \quad (9)$$

where $e^{\beta f_L}$ is an irrelevant constant for a given Hamiltonian, which can be canceled in normalization. In a “traditional” unbiased TP calculation, all samples have equal weights, which is actually a special case of Eq. 9. Suppose we have performed a series of brutal-force unbiased simulations to sample the configurational phase covering the reactant, the product and in between. $W_k = 0$ for all the snapshots, $f_k^{(b)}$ becomes the unbiased free energy, and the exponential terms in the numerator and denominator cancel each other. We find $w_L = 1 / \sum_{k=1}^S N_k = 1/N$, indicating that all the samples have equal weights in a “traditional” unbiased TP calculation.

For a certain histogram bin, the free energy difference between the high-level and low-level Hamiltonians can be obtained via

$$\begin{aligned}
\Delta F(\eta) &= -\frac{1}{\beta} \ln \frac{\sum_{i=1}^S \sum_{l=1}^{N_i} w_L(\mathbf{x}_\eta) \delta(\eta_{(i,l)} - \eta) e^{-\beta[U_H(\mathbf{x}_\eta) - U_L(\mathbf{x}_\eta)]}}{\sum_{i=1}^S \sum_{l=1}^{N_i} w_L(\mathbf{x}_\eta) \delta(\eta_{(i,l)} - \eta)} \\
&= -\frac{1}{\beta} \ln \frac{\sum_{i=1}^S \sum_{l=1}^{N_i} w_L(\mathbf{x}_{\eta_{(i,l)}}) e^{-\beta[U_H(\mathbf{x}_{\eta_{(i,l)}}) - U_L(\mathbf{x}_{\eta_{(i,l)}})]}}{\sum_{i=1}^S \sum_{l=1}^{N_i} w_L(\mathbf{x}_{\eta_{(i,l)}})}, \tag{10}
\end{aligned}$$

where the subscripts H and L denote the high-level and the low-level Hamiltonians, respectively, $\eta_{(i,l)}$ is the histogram bin that the l th configuration in the i th biased simulation belongs to, and $w_L(\mathbf{x}_\eta)$ is the unbiased weight of the sample in bin η under the low-level Hamiltonian. Here, the delta function singles out the samples inside bin η . Actually, we can also calculate the weights of the samples under the high-level Hamiltonian, and then compute the free energy difference between the low-level Hamiltonian and the high level Hamiltonian. Or we can compute the free energy via BAR by calculating the weights of the samples under both the low-level and high-level Hamiltonians. All these calculations will yield the same results as shown in SI.

In order to obtain the uncertainty $\delta^2 \Delta F(\eta)$, Eq. 10 can be divided into two terms as

$$\begin{aligned}
\Delta F(\eta) &= -\frac{1}{\beta} \ln \sum_{i=1}^S \sum_{l=1}^{N_i} w_L(\mathbf{x}_{\eta_{(i,l)}}) e^{-\beta[U_H(\mathbf{x}_{\eta_{(i,l)}}) - U_L(\mathbf{x}_{\eta_{(i,l)}})]} \\
&\quad + \frac{1}{\beta} \ln \sum_{i=1}^S \sum_{l=1}^{N_i} w_L(\mathbf{x}_{\eta_{(i,l)}}). \tag{11}
\end{aligned}$$

The uncertainty $\delta^2 \Delta F(\eta)$ can be computed by error propagation

$$\delta^2 \Delta F(\eta) = \delta_I^2 + \delta_{II}^2. \tag{12}$$

Here, δ_I^2 and δ_{II}^2 correspond to the first and the second terms on the right-hand side of Eq. 11, respectively.

$$\delta_I^2 = \frac{1}{\beta^2} \cdot \frac{1}{\left(\sum_{i=1}^S \sum_{l=1}^{N_i} \delta(\eta_{(i,l)} - \eta) \right)^2} \cdot \frac{\sigma_{y_{i,l}^1}^2}{\langle y_{i,l}^1 \rangle^2}, \quad (13)$$

where $y_{i,l}^1 = w_L(\mathbf{x}_{\eta_{(i,l)}}) e^{-\beta[U_H(\mathbf{x}_{\eta_{(i,l)}}) - U_L(\mathbf{x}_{\eta_{(i,l)}})]}$, $\sum_{i=1}^S \sum_{l=1}^{N_i} \delta(\eta_{(i,l)} - \eta)$ is the number of configurations falling into bin η among the samples from all the biased simulations.

$$\delta_{II}^2 = \frac{1}{\beta^2} \cdot \frac{1}{\left(\sum_{i=1}^S \sum_{l=1}^{N_i} \delta(\eta_{(i,l)} - \eta) \right)^2} \cdot \frac{\sigma_{y_{i,l}^2}^2}{\langle y_{i,l}^2 \rangle^2}, \quad (14)$$

where $y_{i,l}^2 = w_i(\mathbf{x}_{\eta_{(i,l)}})$, $\sum_{i=1}^S \sum_{l=1}^{N_i} \delta(\eta_{(i,l)} - \eta)$ is the number of configurations pertaining to histogram bin η among all the samples.

In this work, the US samplings were performed at the low-level Hamiltonian, of which the FE profile $F_L(\eta)$ can be obtained. Then, the FE profile of the high-level Hamiltonian can be calculated by

$$F_H(\eta) = F_L(\eta) + \Delta F(\eta). \quad (15)$$

The corresponding uncertainty of $F_H(\eta)$ can be computed by error propagation

$$\delta^2 F_H(\eta) = \delta^2 F_L(\eta) + \delta^2 \Delta F(\eta). \quad (16)$$

In the following, we will use direct FE profile to refer to the FE profile obtained from the US samplings at the corresponding Hamiltonian, and use indirect FE profile to refer to the one obtained from TP calculations based on a direct FE profile from a lower-level Hamiltonian.

In order to characterize the reliability of the TP calculation, “reweighting entropy” is

introduced in our previous work,³⁹ which is defined as

$$\mathcal{S}(\eta) = -\frac{1}{\ln \left(\sum_{i=1}^S \sum_{l=1}^{N_i} \delta(\eta_{(i,l)} - \eta) \right)} \sum_{i=1}^S \sum_{l=1}^{N_i} \mathcal{P}(\eta_{(i,l)}) \ln \mathcal{P}(\eta_{(i,l)}), \quad (17)$$

where

$$\mathcal{P}(\eta_{(i,l)}) = \frac{w_L(\mathbf{x}_{\eta_{(i,l)}}) e^{-\beta[U_H(\mathbf{x}_{\eta_{(i,l)}}) - U_L(\mathbf{x}_{\eta_{(i,l)}})]}}{\sum_{i=1}^S \sum_{l=1}^{N_i} w_L(\mathbf{x}_{\eta_{(i,l)}}) e^{-\beta[U_H(\mathbf{x}_{\eta_{(i,l)}}) - U_L(\mathbf{x}_{\eta_{(i,l)}})]}}. \quad (18)$$

Here, $\sum_{i=1}^S \sum_{l=1}^{N_i} \delta(\eta_{(i,l)} - \eta)$ represents the number of configurations falling into bin η among the samples from all the biased simulations. The larger the reweighting entropy is, the more reliable the TP calculation is. \mathcal{S} has a maximum value of 1.0, where all the samples have equal weights. The maximum of $\mathcal{P}(\eta_{(i,l)})$ among $\sum_{i=1}^S \sum_{l=1}^{N_i} \delta(\eta_{(i,l)} - \eta)$ frames is called “maximal weight” \mathcal{P}_{max} . Generally speaking, the smaller the maximal weight is, the more reliable the TP calculation is. It is well known that TP requires significant overlap in phase space between the sampled (PM3 or PM6 in this work) Hamiltonian and the target (PM6 or B3LYP in this work) Hamiltonian.⁶¹

2.3 Gaussian process regression for curve fitting

Gaussian Processes (GP) are generic supervised learning methods designed to solve regression and probabilistic classification problems.⁶² It is an attractive approach because it is nearly model-free. In this work, Gaussian process regression was utilized to fit the free energy profiles after the weighted TP correction, which is doomed to be contaminated by statistical noise. Given a set of observations $\{\Delta F_1, \Delta F_2, \dots, \Delta F_n\}$, it can be imagined as a single sample from a Gaussian distribution with n variates. A Gaussian process is a collection of random variables, any finite number of which have a joint Gaussian distribution. A Gaussian process $f(\eta)$ can be completely specified by its mean $m(\eta)$ and covariance function $k(\eta, \eta')$, expressed

as

$$m(\eta) = E[f(\eta)] \quad (19)$$

and

$$k(\eta, \eta') = E \left[\left(f(\eta) - m(\eta) \right) \left(f(\eta') - m(\eta') \right) \right], \quad (20)$$

where $E[\cdot]$ denotes the expectation operation and the covariance function $k(\eta, \eta')$ relates one observation to another. Since the observations are noisy, each observation ΔF is related to an underlying function $f(\eta)$ through a Gaussian noise model

$$\Delta F = f(\eta) + \mathcal{N}(0, \sigma_n^2). \quad (21)$$

By considering also the noise, the covariance function k was defined using the squared exponential as

$$k(\eta, \eta') = \sigma_f^2 \exp \left[\frac{-(\eta - \eta')^2}{2l^2} \right] + \alpha \sigma_n^2 \delta(\eta, \eta'), \quad (22)$$

where l is the length-scale and σ_f^2 is the signal variance, $\delta(\eta, \eta')$ is the Kronecker delta function and σ_n^2 is the noise variance, which was set to the reciprocal of the exponential of the reweighting entropy value (e^{-S}) corresponding to each observation in this work. The free parameters $\{l, \sigma_f, \alpha\}$ are the “hyperparameters” that are optimized to maximize the likelihood of the observations. The Gaussian process regression was carried out using the scikit-learn package.⁶³

2.4 Molecular Dynamics Simulations

One quasi-chemical reaction and three chemical reactions in aqueous solution shown in Fig. 1 are studied, including main chain dihedral rotation of a butane molecule, an S_N2 reaction of $\text{CH}_3\text{Cl} + \text{Cl}^- \longrightarrow \text{Cl}^- + \text{CH}_3\text{Cl}$, intramolecular proton transfer in glycine from the neutral form to the zwitterion form, and an aliphatic Claisen rearrangement reaction from allyl vinyl ether (AVE) to 4-pentenal.

For the main chain dihedral rotation of a butane molecule, the entire molecule was defined as the semiempirical QM (SQM) or QM region. For the S_N2 reaction, the complex of CH_3Cl and Cl^- was defined as the semiempirical QM (SQM) or QM region. For the glycine intramolecular proton transfer reaction, the glycine molecule was defined as the SQM or QM region. For the Claisen rearrangement reaction, the solute was defined as the SQM or QM region. A TIP3P water sphere with a radius of 25 Å was added to the solute centering on the heavy atom closest to the center-of-mass of the QM regions and was restrained by a soft half-harmonic potential with a force constant of 10 kcal/mol/Å² to avoid evaporation. Thiel et al. have justified the widespread use of a droplet model in QM/MM studies of reactions in solution and in enzymes.⁶⁴ The nonbonded interactions were fully counted without any truncations. The van der Waals (vdW) interactions were described with the general AMBER force field.⁶⁵ PM3 and PM6 were used as the low-level Hamiltonians, and the high-level QM Hamiltonian was chosen as B3LYP/6-31G(d). The umbrella samplings were performed at both PM3 and PM6 levels. We first compared the direct FE profile at PM6 with the indirect one at the same level reweighted from PM3 level. Then, the direct free energy profile at B3LYP/6-31G(d) level was computed to validate the indirect FE profile at the same level reweighted from the SE levels.

For the main chain dihedral rotation of a butane molecule, the main chain dihedral $\eta = \phi\{\text{C1} - \text{C2} - \text{C3} - \text{C4}\}$ was chosen as the reaction coordinate. Umbrella samplings with 61 windows centering on η ranged from 0 to 180 degrees were performed. The reaction coordinate for the S_N2 reaction was defined as $\eta = d_{\text{CCl1}} - d_{\text{CCl2}}$, where d_{CCl1} and d_{CCl2} are

the bond distances. Umbrella samplings with 73 windows centering on η ranged from -2.5 to 2.5 Å were performed. The reaction coordinate for the glycine intramolecular proton transfer reaction was defined as $\eta = d_{OH} - d_{NH}$, where H is the hydrogen atom to be transferred. Umbrella samplings with 61 windows under PM3 level and with 51 windows under PM6 and B3LYP levels centering from on η ranged from -1.5 to 1.5 Å were applied. The reaction coordinate for the Claisen rearrangement reaction was defined as $\eta = d_{OC5} - d_{C2C3}$. Umbrella samplings with 95 windows centering on η ranged from -2.2 to 1.7 Å were applied. For each US window simulation, the system was optimized in energy for 500 steps using the steepest decent optimization method followed by 500 steps of the conjugate gradient method with the respective Hamiltonian. For SE Hamiltonian, the system was heated up to 300 K in 50 ps and was equilibrated for 100 ps. A 1-ns production simulation was conducted for each window for free energy analysis. However, for B3LYP Hamiltonian the system was heated up to 300 K in 10 ps and was equilibrated for 10 ps. The production simulation has a length of 100-ps for each window. The integration time step was set to 1 fs, except for that in the PM3 and B3LYP simulations of the glycine intramolecular proton transfer reaction, which was set to 0.5 fs. The configurations were saved every 0.1 ps in the PM3 and PM6 simulations, and were saved every 0.05 ps in the B3LYP simulations. The temperature was regulated at 300 K with the Andersen temperature coupling scheme.⁶⁶ All the simulations were performed by the AmberTools 16 program package,⁶⁷ and the QM/MM calculations were carried out by interfacing with Q-Chem 4.3 package.⁶⁸

3 Results and Discussion

3.1 Main chain dihedral rotation of a butane molecule

Although the minimal free energy structures are located in the same position in RC under PM3/MM and PM6/MM Hamiltonians, the well depths are different. For the global minimum with $\phi = 180^\circ$, these two Hamiltonians differ by 0.2 kcal/mol. The other free

energy minimum is located at $\phi = 68.5^\circ$. The well depth from the PM3/MM calculation is -3.39 kcal/mol, which is 0.4 kcal/mol deeper than that from the PM6/MM calculation (-2.99 kcal/mol). Although the weighted TP correction was rigorously derived, its practical applicability is still worth a validation. In the first step, the PM3-to-PM6 correction was applied to the direct PM3 FE profile, and the indirect PM6 FE profile obtained in this way was compared with the direct PM6 FE profile. As shown in Fig. S3, all the reweighting entropy values are larger than 0.76, which indicate that this TP calculation is trustworthy and a smooth indirect FE profile can be obtained. It clearly shows in Fig. 2 that the indirect PM6 FE profile is highly consistent with the direct PM6 FE profile, indicating that the reweighting method introduced in this work is not only theoretically rigorous but also practically reliable at least for the correction from PM3 to PM6.

Next, the PM3-to-B3LYP and PM6-to-B3LYP corrections were applied to generate the indirect FE profiles at the B3LYP level. As shown in Fig. S3, the reweighting entropies are smaller than those in the TP calculations from PM3 to PM6, indicating that the overlaps in phase space between B3LYP and the SQM Hamiltonians are less significant than that between PM3 and PM6, and the TP corrections from SQM to B3LYP were less numerically robust. Comparing with PM3, the PM6 Hamiltonian was closer to B3LYP as can be inferred from the reweighting entropy values. This is reasonable, because PM6 was refined over the PM3 Hamiltonian. Nevertheless, most of the weighting entropy values are still larger than 0.6, with only a small number of exceptions. It can be noted that at $\phi = 180^\circ$, there is a precipitous drop of reweighting entropy in reweighting the PM3 level to the B3LYP level process in Fig. S3, which leads to a corresponding precipitous drop of the free energy around this region as shown in Fig. S4. This indicates that the weighted TP corrections for each histogram bin is sensitive to the reweighting entropy quantity, and the reweighting entropy can be used to characterize the reliability of the weighted TP calculations. Then, we fitted these two indirect FE profiles by Gaussian process regression, and the smoothed curves are nearly identical except for a small difference near $\phi = 180^\circ$, as shown in Fig. 3. They are

also very close to the direct FE profile at the same level, and the indirect one from the PM6 level performs slightly better than the indirect one corrected from the PM3 level. The two indirect B3LYP FE profiles reweighted from the PM3 and PM6 levels have a free energy of -6.18 kcal/mol and -5.83 kcal/mol at $\phi = 180^\circ$, respectively. The direct FE profile has a free energy of -5.86 ± 0.11 kcal/mol at $\phi = 180^\circ$. Meanwhile, all the B3LYP FE profiles, either direct or indirect, have the same positions in RC for the maximal and minimal free energy structures.

3.2 S_N2 reaction of $\text{CH}_3\text{Cl} + \text{Cl}^- \longrightarrow \text{Cl}^- + \text{CH}_3\text{Cl}$

As shown in Fig. 4, the direct FE profile calculated at the PM3 level shows some difference from that at the PM6 level. The free energy barrier estimated from the PM3 simulations is about 4.7 kcal/mol higher than that obtained from the PM6 simulations. The element-specific Gaussian core-core corrections in PM3 is replaced with a pairwise core-core correction term in PM6.⁶⁹ Besides, *d*-orbitals are added to the atomic basis for certain elements including chlorine in the PM6 Hamiltonian, which shows significant improvement over the PM3 method.⁷⁰ Therefore, it is expected that PM6 Hamiltonian outperforms PM3 for the agreement of the FE profile with the one at the B3LYP level. After the PM3-to-PM6 correction, the indirect PM6 FE profile is highly consistent with the direct PM6 FE profile, as shown in Fig. 4. The reweighting entropies are all larger than 0.70 (see Fig. S7), which also indicates that this TP calculation can generate a reliable indirect FE curve.

However, when running the TP calculations from the SQM to B3LYP level, the reweighting entropies became much smaller than those in the PM3-to-PM6 TP corrections (see Fig. S7). This is caused by the slow convergence at the tail region of the biasing potential distribution.^{40,61,71–74} It can be imagined that the fitted FE profile data are noisy, which are shown in Fig. S8. This statistical fluctuation can be well smoothed by the Gaussian process regression, and the final curves are nearly identical, as shown in Fig. 5. In addition, these two indirect B3LYP FE profiles are highly consistent with the direct B3LYP FE profile, except

for some marginal difference at the transition state and product state regions. Especially, when corrected from the PM6 level, the transition barrier differs by only 0.45 kcal/mol from the direct FE profile at the B3LYP level.

3.3 Glycine intramolecular proton transfer reaction

As shown in Fig. 6, the FE profile calculated at the PM3 level is very different from that at the PM6 level. The reaction free energy and activation barrier estimated from the PM3/MM MD simulations are 1.51 ± 0.11 and 24.47 ± 0.08 kcal/mol, respectively, while those obtained from the PM6/MM simulations are -13.45 ± 0.08 and 3.25 ± 0.05 kcal/mol. The transition state at PM3 level is located at -0.02 \AA , while that at PM6 level is located at -0.36 \AA . Obviously, the PM3/MM simulations yielded an incorrect result, because the zwitterion form of glycine molecule is stabilized by the water molecules and is the dominant form in aqueous solution. The glycine intramolecular proton transfer reaction process involves one hydrogen atom transferred from the oxygen atom to the nitrogen atom. Because PM6 uses different core-core repulsion potentials for N-H, O-H, C-C, Si-O pairs to correct for the specific weakness in the parametrization, it is not surprising that it yielded a FE profile that is much better than the PM3 one. As is shown in Fig. S11, some of the reweighting entropies are rather small in magnitude in comparison with those obtained for the two systems above, especially for the bins with RC from -1.5 \AA to -0.5 \AA . After the TP correction, the indirect PM6 FE profile shows some deviations from the direct one in this region. It is interesting to see that after the Gaussian process regression, the indirect PM6 FE profile can be well superimposed with the direct PM6 FE profile. This result demonstrated that this TP correction can even work well in fixing this large difference in Hamiltonians.

The reweighting entropies are even smaller in the TP calculations from the PM3 and PM6 levels to the B3LYP level as shown in Fig. S11, which leads to even noisy FE profiles as shown in Fig. S12. Because PM3 is worse than PM6, it is quite natural that the indirect FE profile from PM3 has much more notable fluctuations than the one from PM6. After

Gaussian process regression, the curves agree much better with each other, as well as the direct FE profile at the B3LYP level as shown in Fig. 7. The transition states after TP correction shift to the left by 0.09 Å (at -0.11 Å) for PM3 and to the right by 0.2 Å (at -0.16 Å) for PM6 as compared to the original SQM results. The transition state in the direct B3LYP FE profile locates at -0.11 Å. The free energy barrier heights in the indirect FE profiles are 2.79 kcal/mol and 3.67 kcal/mol, respectively, which are close to the direct B3LYP FE profile (3.04 kcal/mol) with somewhat acceptable difference.

3.4 Aliphatic Claisen rearrangement reaction of allyl vinyl ether (AVE) to 4-pentenal

Just like the other three reactions, the PM3 FE profile shows some difference from the PM6 one. The reaction barrier is about 5.0 kcal/mol higher (30.42 ± 0.08 kcal/mol for PM6 v.s. 35.43 ± 0.08 kcal/mol for PM3), and the reaction free energy is 10.5 kcal/mol more negative (-14.88 ± 0.11 kcal/mol for PM6 vs -25.39 ± 0.12 kcal/mol for PM3). However, the TP correction can still eliminate this difference, and the direct and indirect PM6 FE profiles agree with each other quite well with only marginal difference in some small region as shown in Fig. S14, which was mainly caused by the small magnitude of the reweighting entropy in these regions as shown in Fig. S15. Most of the bins have a reweighting entropy larger than 0.6, which guaranteed reliable free energy corrections for those bins. After smoothing using the Gaussian process regression, the direct and indirect FE profiles at PM6 level perfectly agree with each, as shown in Fig. 8.

In the TP calculations from the PM3 and PM6 levels to the B3LYP level, the reweighting entropies are even smaller, resulting in two rough indirect FE profiles at the B3LYP level shown in Fig. S16. For the indirect FE profile from PM6, the noise is rather intense in the region with the RC around 0.0 Å, which corresponds well with the small reweighting entropy in that region as shown in Fig. S15. The two indirect B3LYP FE profiles after being smoothed by the Gaussian process regression method are highly consistent with each other

again, which are shown in Fig. 9. The transition states after the TP corrections from the PM3 and PM6 Hamiltonians are located at -0.42 Å and -0.32 Å, respectively, which are shifted to the left by 0.15 Å and 0.05 Å as compared to the original SQM results. The transition state in the direct B3LYP/MM FE profile locates at -0.46 Å. The free energy barrier height in the indirect FE profiles are 27.48 kcal/mol and 28.05 kcal/mol, which deviate by only 4 percent and 7 percent from the direct B3LYP/MM simulation (26.30 kcal/mol).

3.5 Computational expense

The estimated wall times for the computations of the QM/MM free energy profiles at the B3LYP/6-31G* level are listed in Table 1. For the calculations of the indirect profiles, the wall time include both the time for generating the SQM trajectories and the time for the single point calculations at the B3LYP level. The cost at the PM3 level is similar to that at the PM6 level with the S_N2 reaction being an exception, which was caused by the additional d -orbital in the basis set for the chlorine atoms in PM6. Nonetheless, both methods are orders of magnitude faster than the direct calculations of the profiles at the B3LYP level. Because the samples for the single-point calculations at the B3LYP level were saved once every 100 MD steps in the SQM simulations in this work, the efficiency enhancement cannot exceed 100 folds. The samples can be saved every 1000 steps or even less infrequently, especially for chemical reactions with a correlation time longer than tens of picoseconds. Then, the enhancement in the efficiency will be even greater.

4 Conclusion

For chemical reactions in condensed phase or enzymatic reactions, the computation of a converged free energy (FE) profile at *ab initio* (*ai*) QM/MM level is still far from being affordable. In this work, we proposed a new method termed MBAR+wTP to obtain the FE profile at *ai* QM/MM level with much less computational expense by combining the

Multistate Bennett Acceptance Ratio (MBAR) method and weighted Thermodynamic Perturbation (TP) method. This method uses the semiempirical (SE) QM/MM free energy profile obtained from MBAR analysis of the Umbrella Sampling (US) trajectories as an initial guess, followed by the SE-to-*ai* correction using weighted TP. One quasi-chemical reaction and three chemical reactions are used to validate the applicability of this method. The SE FE profiles may deviate from the *ai* ones by several kcal/mol in terms of the barrier height and the reaction free energy. After the SE-to-*ai* correction, the FE profiles can agree much better with the direct simulated one with errors below 1 kcal/mol for most cases. Numerical difficulty in the weighted TP calculations are inevitable, similar to most TP calculations. However, curve fitting using the Gaussian process regression can effectively reduce the impact of the fluctuations caused by the numerical difficulty. Choosing a SE method that is closer to the *ai* Hamiltonian may reduce the fluctuation and make this method more reliable. Because the samples used for the TP calculations are only one hundredth or even one thousandth of the total number of samples generated in the simulation, this method can increase the efficiency by several orders of magnitude. Because the numerical difficulty increases with the complexity of the reactions, we will valid this approach further by applying it in some real systems like enzymatic reactions.

Acknowledgement

This work is supported by the National Natural Science Foundation of China (Grant No. 21773066) and the Fundamental Research Funds for the Central Universities. CPU time was provided by the Supercomputer Center of East China Normal University.

References

- (1) Hu, H.; Yang, W. Free Energies of Chemical Reactions in Solution and in Enzymes with *ab initio* Quantum Mechanics/Molecular Mechanics Methods. *Annu. Rev. Phys. Chem.* **2008**, *59*, 573–601.
- (2) Laidler, K. J.; King, M. C. Development of Transition-State Theory. *J. Phys. Chem.* **1983**, *87*, 2657–2664.
- (3) Truhlar, D. G.; Garrett, B. C.; Klippenstein, S. J. Current Status of Transition-State Theory. *J. Phys. Chem.* **1996**, *100*, 12771–12800.
- (4) Shirts, M. R.; Chodera, J. D. Statistically Optimal Analysis of Samples from Multiple Equilibrium States. *J. Chem. Phys.* **2008**, *129*, 124105.
- (5) Shirts, M. R. Reweighting from the Mixture Distribution as a Better Way to Describe the Multistate Bennett Acceptance Ratio. arXiv.org, 2017; <https://arxiv.org/abs/1704.00891>.
- (6) Ferrenberg, A. M.; Swendsen, R. H. Optimized Monte Carlo Data Analysis. *Phys. Rev. Lett.* **1989**, *63*, 1195–1198.
- (7) Souaille, M.; Roux, B. Extension to the Weighted Histogram Analysis Method: Combining Umbrella Sampling with Free Energy Calculations. *Comput. Phys. Commun.* **2001**, *135*, 40–57.
- (8) Gallicchio, E.; Andrec, M.; Felts, A. K.; Levy, R. M. Temperature Weighted Histogram Analysis Method, Replica Exchange, and Transition Paths. *J. Phys. Chem. B* **2005**, *109*, 6722–6731.
- (9) Chodera, J. D.; Swope, W. C.; Pitera, J. W.; Seok, C.; Dill, K. A. Use of the Weighted Histogram Analysis Method for the Analysis of Simulated and Parallel Tempering Simulations. *J. Chem. Theory Comput.* **2007**, *3*, 26–41.

- (10) Mey, A. S. J. S.; Wu, H.; Noé, F. xTRAM: Estimating Equilibrium Expectations from Time-Correlated Simulation Data at Multiple Thermodynamic States. *Phys. Rev. X* **2014**, *4*, 041018.
- (11) Warshel, A.; Levitt, M. Theoretical Studies of Enzymic Reactions: Dielectric, Electrostatic and Steric Stabilization of the Carbonium Ion in the Reaction of Lysozyme. *J. Mol. Biol.* **1976**, *103*, 227–249.
- (12) Zhang, Y.; Lee, T.-S.; Yang, W. A Pseudobond Approach to Combining Quantum Mechanical and Molecular Mechanical Methods. *J. Chem. Phys.* **1999**, *110*, 46–54.
- (13) Zhang, Y.; Liu, H.; Yang, W. Free Energy Calculation on Enzyme Reactions with an Efficient Iterative Procedure to Determine Minimum Energy Paths on a Combined *ab initio* QM/MM Potential Energy Surface. *J. Chem. Phys.* **2000**, *112*, 3483–3492.
- (14) Cui, Q.; Karplus, M. Triosephosphate Isomerase: A Theoretical Comparison of Alternative Pathways. *J. Am. Chem. Soc.* **2001**, *123*, 2284–2290.
- (15) Stewart, J. J. P. Optimization of Parameters for Semiempirical Methods I. Method. *J. Comput. Chem.* **1989**, *10*, 209–220.
- (16) Dewar, M. J. S.; Zoebisch, E. G.; Healy, E. F.; Stewart, J. J. P. Development and Use of Quantum Mechanical Molecular Models. 76. AM1: A New General Purpose Quantum Mechanical Molecular Model. *J. Am. Chem. Soc.* **1985**, *107*, 3902–3909.
- (17) Dewar, M. J. S.; Thiel, W. Ground States of Molecules. 38. The MNDO Method. Approximations and Parameters. *J. Am. Chem. Soc.* **1977**, *99*, 4899–4907.
- (18) Stewart, J. J. P. Optimization of Parameters for Semiempirical Methods V: Modification of NDDO Approximations and Application to 70 Elements. *J. Mol. Model.* **2007**, *13*, 1173–1213.

- (19) Warshel, A.; Weiss, R. M. An Empirical Valence Bond Approach for Comparing Reactions in Solutions and in Enzymes. *J. Am. Chem. Soc.* **1980**, *102*, 6218–6226.
- (20) Warshel, A. *Computer Modeling of Chemical Reactions in Enzymes and Solutions*; John Wiley and Sons: New York, 1991.
- (21) Billeter, S.; Webb, S.; Iordanov, T.; Agarwal, P.; Hammes-Schiffer, S. Hybrid Approach for Including Electronic and Nuclear Quantum Effects in Molecular Dynamics Simulations of Hydrogen Transfer Reactions in Enzymes. *J. Chem. Phys.* **2001**, *114*, 6925–6936.
- (22) Porezag, D.; Frauenheim, T.; Kohler, T.; Seifert, G.; Kaschner, R. Construction of Tight-Binding-Like Potentials on the Basis of Density-Functional-Theory: Applications to Carbon. *Phys. Rev. B* **1995**, *51*, 12947.
- (23) Seabra, G. d. M.; Walker, R. C.; Elstner, M.; Case, D. A.; Roitberg, A. E. Implementation of the SCC-DFTB Method for Hybrid QM/MM Simulations within the Amber Molecular Dynamics Package. *J. Phys. Chem. A* **2007**, *111*, 5655–5664.
- (24) Elstner, M.; Porezag, D.; Jungnickel, G.; Elsner, J.; Haugk, M.; Frauenheim, T.; Suhai, S.; Seifert, G. Self-consistent Charge Density Functional Tight-Binding Method for Simulation of Complex Material Properties. *Phys. Rev. B* **1998**, *58*, 7260.
- (25) Christensen, A. S.; Kromann, J. C.; Jensen, J. H.; Cui, Q. Intermolecular Interactions in the Condensed Phase: Evaluation of Semi-empirical Quantum Mechanical Methods. *J. Chem. Phys.* **2017**, *147*, 161704.
- (26) Gao, J. Absolute Free Energy of Solvation from Monte Carlo Simulations Using Combined Quantum and Molecular Mechanical Potentials. *J. Phys. Chem.* **1992**, *96*, 537–540.

- (27) Gao, J.; Xia, X. A Priori Evaluation of Aqueous Polarization Effects through Monte Carlo QM-MM Simulations. *Science* **1992**, *258*, 631–635.
- (28) Bentzien, J.; Muller, R. P.; Florián, J.; Warshel, A. Hybrid *ab initio* Quantum Mechanics/Molecular Mechanics Calculations of Free Energy Surfaces for Enzymatic Reactions: The Nucleophilic Attack in Subtilisin. *J. Phys. Chem. B* **1998**, *102*, 2293–2301.
- (29) Plotnikov, N. V.; Kamerlin, S. C. L.; Warshel, A. Paradynamics: An Effective and Reliable Model for *ab initio* QM/MM Free-Energy Calculations and Related Tasks. *J. Phys. Chem. B* **2011**, *115*, 7950–7962.
- (30) Plotnikov, N. V.; Warshel, A. Exploring, Refining, and Validating the Paradynamics QM/MM Sampling. *J. Phys. Chem. B* **2012**, *116*, 10342–10356.
- (31) Lameira, J.; Kupchenko, I.; Warshel, A. Enhancing Paradynamics for QM/MM Sampling of Enzymatic Reactions. *J. Phys. Chem. B* **2016**, *120*, 2155–2164.
- (32) Rod, T. H.; Ryde, U. Quantum Mechanical Free Energy Barrier for an Enzymatic Reaction. *Phys. Rev. Lett.* **2005**, *94*, 138302.
- (33) Beierlein, F. R.; Michel, J.; Essex, J. W. A Simple QM/MM Approach for Capturing Polarization Effects in Protein-ligand Binding Free Energy Calculations. *J. Phys. Chem. B* **2011**, *115*, 4911–4926.
- (34) Polyak, I.; Benighaus, T.; Boulanger, E.; Thiel, W. Quantum Mechanics/Molecular Mechanics Dual Hamiltonian Free Energy Perturbation. *J. Chem. Phys.* **2013**, *139*, 064105.
- (35) König, G.; Boresch, S. Non-Boltzmann Sampling and Bennett’s Acceptance Ratio Method: How to Profit from Bending the Rules. *J. Comput. Chem.* **2011**, *32*, 1082–1090.

- (36) König, G.; Hudson, P. S.; Boresch, S.; Woodcock, H. L. Multiscale Free Energy Simulations: An Efficient Method for Connecting Classical MD Simulations to QM or QM/MM Free Energies Using Non-Boltzmann Bennett Reweighting Schemes. *J. Chem. Theory Comput.* **2014**, *10*, 1406–1419.
- (37) Hudson, P. S.; White, J. K.; Kearns, F. L.; Hodoscek, M.; Boresch, S.; Lee Woodcock, H. Efficiently Computing Pathway Free Energies: New Approaches Based on Chain-of-replica and Non-Boltzmann Bennett Reweighting Schemes. *BBA Gen. Subjects* **2015**, *1850*, 944–953.
- (38) Hudson, P. S.; Woodcock, H. L.; Boresch, S. Use of Nonequilibrium Work Methods to Compute Free Energy Differences Between Molecular Mechanical and Quantum Mechanical Representations of Molecular Systems. *J. Phys. Chem. Lett.* **2015**, *6*, 4850–4856.
- (39) Wang, M.; Li, P.; Jia, X.; Liu, W.; Shao, Y.; Hu, W.; Zheng, J.; Brooks, B. R.; Mei, Y. Efficient Strategy for the Calculation of Solvation Free Energies in Water and Chloroform at the Quantum Mechanical/Molecular Mechanical Level. *J. Chem. Inf. Model.* **2017**, *57*, 2476–2489.
- (40) Jia, X.; Wang, M.; Shao, Y.; König, G.; Brooks, B. R.; Zhang, J. Z. H.; Mei, Y. Calculations of Solvation Free Energy through Energy Reweighting from Molecular Mechanics to Quantum Mechanics. *J. Chem. Theory Comput.* **2016**, *12*, 499–511.
- (41) Dybeck, E. C.; König, G.; Brooks, B. R.; Shirts, M. R. Comparison of Methods To Reweight from Classical Molecular Simulations to QM/MM Potentials. *J. Chem. Theory Comput.* **2016**, *12*, 1466–1480.
- (42) Rupp, M. Special Issue on Machine Learning and Quantum Mechanics. *Int. J. Quantum Chem.* **2015**, *115*, 1003–1004.

- (43) Goh, G. B.; Hodas, N. O.; Vishnu, A. Deep Learning for Computational Chemistry. *J. Comput. Chem.* **2017**, *38*, 1291–1307.
- (44) Handley, C. M.; Popelier, P. L. A. Potential Energy Surfaces Fitted by Artificial Neural Networks. *J. Phys. Chem. A* **2010**, *114*, 3371–3383.
- (45) Caccin, M.; Li, Z.; Kermode, J. R.; De Vita, A. A Framework for Machine-learning-augmented Multiscale Atomistic Simulations on Parallel Supercomputers. *Int. J. Quantum Chem.* **2015**, *115*, 1129–1139.
- (46) Ramakrishnan, R.; Dral, P. O.; Rupp, M.; von Lilienfeld, O. A. Big Data Meets Quantum Chemistry Approximations: The Δ -Machine Learning Approach. *J. Chem. Theory Comput.* **2015**, *11*, 2087–2096.
- (47) Botu, V.; Batra, R.; Chapman, J.; Ramprasad, R. Machine Learning Force Fields: Construction, Validation, and Outlook. *J. Phys. Chem. C* **2017**, *121*, 511–522.
- (48) Shen, L.; Wu, J.; Yang, W. Multiscale Quantum Mechanics/Molecular Mechanics Simulations with Neural Networks. *J. Chem. Theory Comput.* **2016**, *12*, 4934–4946.
- (49) Wu, J.; Shen, L.; Yang, W. Internal Force Corrections with Machine Learning for Quantum Mechanics/Molecular Mechanics Simulations. *J. Chem. Phys.* **2017**, *147*, 161732.
- (50) Dral, P. O.; Owens, A.; Yurchenko, S. N.; Thiel, W. Structure-based Sampling and Self-correcting Machine Learning for Accurate Calculations of Potential Energy Surfaces and Vibrational Levels. *J. Chem. Phys.* **2017**, *146*, 244108.
- (51) Li, Y.; Li, H.; Pickard, F. C.; Narayanan, B.; Sen, F. G.; Chan, M. K. Y.; Sankaranarayanan, S. K. R. S.; Brooks, B. R.; Roux, B. Machine Learning Force Field Parameters from Ab Initio Data. *J. Chem. Theory Comput.* **2017**, *13*, 4492–4503.

- (52) Gonzalez-Lafont, A.; Truong, T. N.; Truhlar, D. G. Direct Dynamics Calculations with NDDO (Neglect of Diatomic Differential Overlap) Molecular Orbital Theory with Specific Reaction Parameters. *J. Phys. Chem.* **1991**, *95*, 4618–4627.
- (53) Nam, K.; Cui, Q.; Gao, J.; York, D. M. Specific Reaction Parametrization of the AM1/d Hamiltonian for Phosphoryl Transfer Reactions: H, O, and P Atoms. *J. Chem. Theory Comput.* **2007**, *3*, 486–504.
- (54) Doron, D.; Major, D. T.; Kohen, A.; Thiel, W.; Wu, X. Hybrid Quantum and Classical Simulations of the Dihydrofolate Reductase Catalyzed Hydride Transfer Reaction on an Accurate Semi-Empirical Potential Energy Surface. *J. Chem. Theory Comput.* **2011**, *7*, 3420–3437.
- (55) Zhou, Y.; Pu, J. Reaction Path Force Matching: A New Strategy of Fitting Specific Reaction Parameters for Semiempirical Methods in Combined QM/MM Simulations. *J. Chem. Theory Comput.* **2014**, *10*, 3038–3054.
- (56) Maurer, P.; Laio, A.; Hugosson, H. W.; Colombo, M. C.; Rothlisberger, U. Automated Parametrization of Biomolecular Force Fields from Quantum Mechanics/Molecular Mechanics (QM/MM) Simulations through Force Matching. *J. Chem. Theory Comput.* **2007**, *3*, 628–639.
- (57) Wu, R.; Lu, Z.; Cao, Z.; Zhang, Y. A Transferable Nonbonded Pairwise Force Field to Model Zinc Interactions in Metalloproteins. *J. Chem. Theory Comput.* **2011**, *7*, 433–443.
- (58) Knight, C.; Maupin, C. M.; Izvekov, S.; Voth, G. A. Defining Condensed Phase Reactive Force Fields from ab Initio Molecular Dynamics Simulations: The Case of the Hydrated Excess Proton. *J. Chem. Theory Comput.* **2010**, *6*, 3223–3232.
- (59) Torrie, G.; Valleau, J. Nonphysical Sampling Distributions in Monte Carlo Free-energy Estimation: Umbrella Sampling. *J. Comput. Phys.* **1977**, *23*, 187–199.

- (60) Zwanzig, R. W. High-Temperature Equation of State by a Perturbation Method. I. Nonpolar Gases. *J. Chem. Phys.* **1954**, *22*, 1420.
- (61) Lu, N.; Woolf, T. B. In *Free Energy Calculations*; Chipot, C., Pohorille, A., Eds.; Springer: Heidelberg, 2007; pp 199–247.
- (62) Rasmussen, C.; Williams, C. *Gaussian Processes for Machine Learning*; MIT Press, 2006; pp 7–32.
- (63) Pedregosa, F.; Varoquaux, G.; Gramfort, A.; Michel, V.; Thirion, B.; Grisel, O.; Blondel, M.; Prettenhofer, P.; Weiss, R.; Dubourg, V.; Vanderplas, J.; Passos, A.; Cournapeau, D.; Brucher, M.; Perrot, M.; Duchesnay, E. Scikit-learn: Machine Learning in Python. *J. Mach. Learn. Res.* **2011**, *12*, 2825–2830.
- (64) Vasilevskaya, T.; Thiel, W. Periodic Boundary Conditions in QM/MM Calculations: Implementation and Tests. *J. Chem. Theory Comput.* **2016**, *12*, 3561.
- (65) Wang, J.; Wolf, R. M.; Caldwell, J. W.; Kollman, P. A.; Case, D. A. Development and Testing of a General Amber Force Field. *J. Comput. Chem.* **2004**, *25*, 1157–1174.
- (66) Andrea, T. A.; Swope, W. C.; Andersen, H. C. The Role of Long Ranged Forces in Determining the Structure and Properties of Liquid Water. *J. Chem. Phys.* **1983**, *79*, 4576–4584.
- (67) Case, D. A.; Berryman, J. T.; Betz, R. M.; Cerutti, D. S.; Cheatham, T. E., III; Darden, T. A.; Duke, R. E.; Giese, T. J.; Gohlke, H.; Goetz, A. W.; Homeyer, N.; Izadi, N.; Janowski, P.; Kaus, J.; Kovalenko, A.; Lee, T. S.; LeGrand, S.; Li, P.; Luchko, T.; Luo, R.; Madej, B.; Merz, K. M.; Monard, G.; Needham, P.; Nguyen, H.; Nguyen, H. T.; Omelyan, I.; Onufriev, A.; Roe, D. R.; Roitberg, A.; Salomon-Ferrer, R.; Simmerling, C. L.; Smith, W.; Swails, J.; Walker, R. C.; Wang, J.; Wolf, R. M.; Wu, X.; York, D. M.; Kollman, P. A. AMBER 2016, University of California, San Francisco. 2016.

- (68) Shao, Y.; Gan, Z.; Epifanovsky, E.; Gilbert, A. T.; Wormit, M.; Kussmann, J.; Lange, A. W.; Behn, A.; Deng, J.; Feng, X.; Ghosh, D.; Goldey, M.; Horn, P. R.; Jacobson, L. D.; Kaliman, I.; Khaliullin, R. Z.; Kuś, T.; Landau, A.; Liu, J.; Proynov, E. I.; Rhee, Y. M.; Richard, R. M.; Rohrdanz, M. A.; Steele, R. P.; Sundstrom, E. J.; Woodcock, H. L.; Zimmerman, P. M.; Zuev, D.; Albrecht, B.; Alguire, E.; Austin, B.; Beran, G. J. O.; Bernard, Y. A.; Berquist, E.; Brandhorst, K.; Bravaya, K. B.; Brown, S. T.; Casanova, D.; Chang, C.-M.; Chen, Y.; Chien, S. H.; Closser, K. D.; Crittenden, D. L.; Diedenhofen, M.; DiStasio, R. A.; Do, H.; Dutoi, A. D.; Edgar, R. G.; Fatehi, S.; Fusti-Molnar, L.; Ghysels, A.; Golubeva-Zadorozhnaya, A.; Gomes, J.; Hanson-Heine, M. W.; Harbach, P. H.; Hauser, A. W.; Hohenstein, E. G.; Holden, Z. C.; Jagau, T.-C.; Ji, H.; Kaduk, B.; Khistyayev, K.; Kim, J.; Kim, J.; King, R. A.; Klunzinger, P.; Kosenkov, D.; Kowalczyk, T.; Krauter, C. M.; Lao, K. U.; Laurent, A. D.; Lawler, K. V.; Levchenko, S. V.; Lin, C. Y.; Liu, F.; Livshits, E.; Lochan, R. C.; Luenser, A.; Manohar, P.; Manzer, S. F.; Mao, S.-P.; Mardirossian, N.; Marenich, A. V.; Maurer, S. A.; Mayhall, N. J.; Neuscamman, E.; Oana, C. M.; Olivares-Amaya, R.; O'Neill, D. P.; Parkhill, J. A.; Perrine, T. M.; Peverati, R.; Prociuk, A.; Rehn, D. R.; Rosta, E.; Russ, N. J.; Sharada, S. M.; Sharma, S.; Small, D. W.; Sodt, A.; Stein, T.; Stück, D.; Su, Y.-C.; Thom, A. J.; Tsuchimochi, T.; Vanovschi, V.; Vogt, L.; Vydrov, O.; Wang, T.; Watson, M. A.; Wenzel, J.; White, A.; Williams, C. F.; Yang, J.; Yeganeh, S.; Yost, S. R.; You, Z.-Q.; Zhang, I. Y.; Zhang, X.; Zhao, Y.; Brooks, B. R.; Chan, G. K.; Chipman, D. M.; Cramer, C. J.; Goddard, W. A.; Gordon, M. S.; Hehre, W. J.; Klamt, A.; Schaefer, H. F.; Schmidt, M. W.; Sherrill, C. D.; Truhlar, D. G.; Warshel, A.; Xu, X.; Aspuru-Guzik, A.; Baer, R.; Bell, A. T.; Besley, N. A.; Chai, J.-D.; Dreuw, A.; Dunietz, B. D.; Furlani, T. R.; Gwaltney, S. R.; Hsu, C.-P.; Jung, Y.; Kong, J.; Lambrecht, D. S.; Liang, W.; Ochsenfeld, C.; Rassolov, V. A.; Slipchenko, L. V.; Subotnik, J. E.; Van Voorhis, T.; Herbert, J. M.; Krylov, A. I.; Gill, P. M.; Head-Gordon, M. *Advances in Molecular Quantum Chemistry Contained*

- in the Q-Chem 4 Program Package. *Mol. Phys.* **2015**, *113*, 184–215.
- (69) Christensen, A. S.; Kubař, T.; Cui, Q.; Elstner, M. Semiempirical Quantum Mechanical Methods for Noncovalent Interactions for Chemical and Biochemical Applications. *Chem. Rev.* **2016**, *116*, 5301–5337.
- (70) Thiel, W.; Voityuk, A. A. Extension of MNDO to d Orbitals: Parameters and Results for the Second-Row Elements and for the Zinc Group. *J. Phys. Chem.* **1996**, *100*, 616–626.
- (71) Heimdal, J.; Ryde, U. Convergence of QM/MM Free-Energy Perturbations Based on Molecular-Mechanics or Semiempirical Simulations. *Phys. Chem. Chem. Phys.* **2012**, *14*, 12592–12604.
- (72) König, G.; Hudson, P. S.; Boresch, S.; Woodcock, H. L. Multiscale Free Energy Simulations: An Efficient Method for Connecting Classical MD Simulations to QM or QM/MM Free Energies Using Non-Boltzmann Bennett Reweighting Schemes. *J. Chem. Theory Comput.* **2014**, *10*, 1406–1419.
- (73) Cave-Ayland, C.; Skylaris, C.-K.; Essex, J. W. Direct Validation of the Single Step Classical to Quantum Free Energy Perturbation. *J. Phys. Chem. B* **2015**, *119*, 1017–1025.
- (74) Klimovich, P. V.; Shirts, M. R.; Mobley, D. L. Guidelines for the Analysis of Free Energy Calculations. *J. Comput. Aid. Mol. Des.* **2015**, *29*, 397–411.

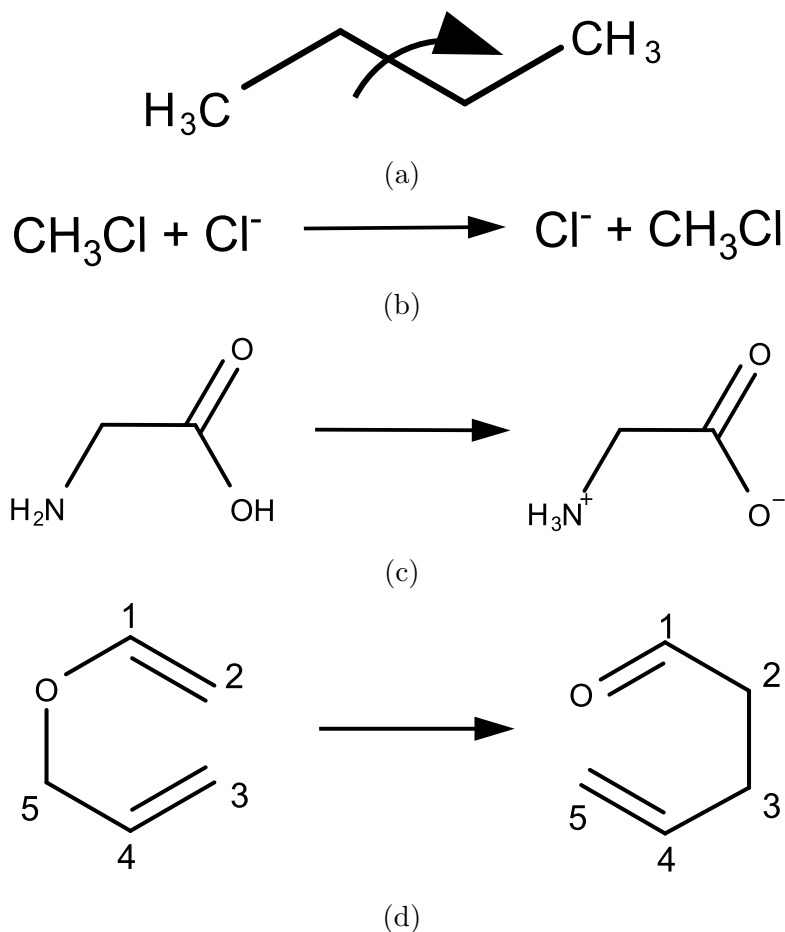


Figure 1: (a) The main chain dihedral rotation of a butane molecule, for which the reaction coordinate was chosen as $\eta = \phi\{C1 - C2 - C3 - C4\}$. (b) The $\text{S}_{\text{N}}2$ reaction of $\text{CH}_3\text{Cl} + \text{Cl}^- \longrightarrow \text{Cl}^- + \text{CH}_3\text{Cl}$, for which the reaction coordinate was chosen as $\eta = d_{\text{CCl1}} - d_{\text{CCl2}}$. (c) The intramolecular proton transfer reaction of glycine from the neutral form (left) to the zwitterion form (right), for which the reaction coordinate was chosen as $\eta = d_{\text{OH}} - d_{\text{NH}}$. (d) The aliphatic Claisen rearrangement reaction of allyl vinyl ether (AVE) (left) to 4-penten-2-one (right), for which reaction coordinate was chosen as $\eta = d_{\text{OC5}} - d_{\text{C2C3}}$.

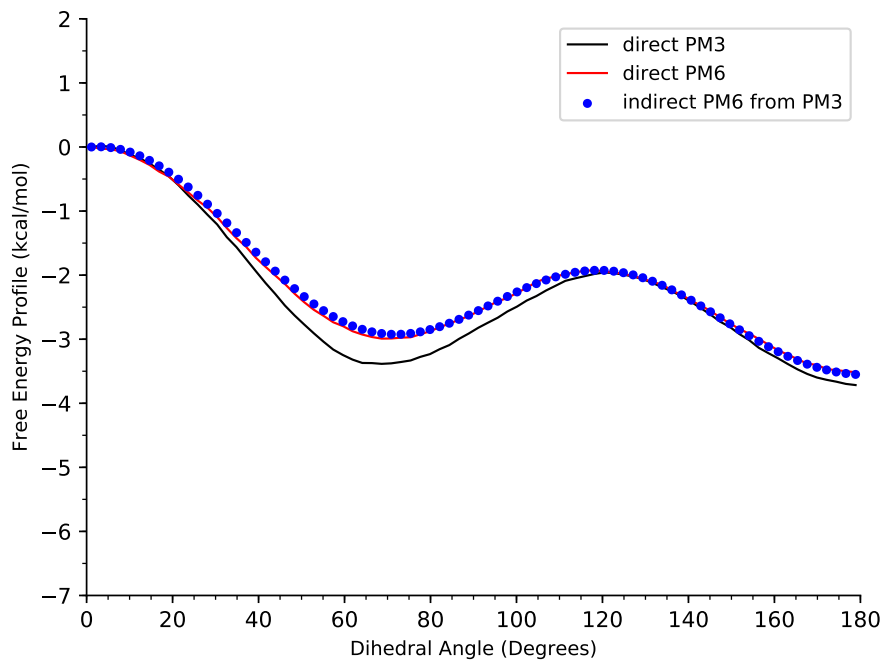


Figure 2: The direct FE profiles for the main chain dihedral rotation of a butane molecule at the PM3 level (black) and the PM6 level (red), as well as the indirect FE profile at the PM6 level corrected from the PM3 curve (blue dots).

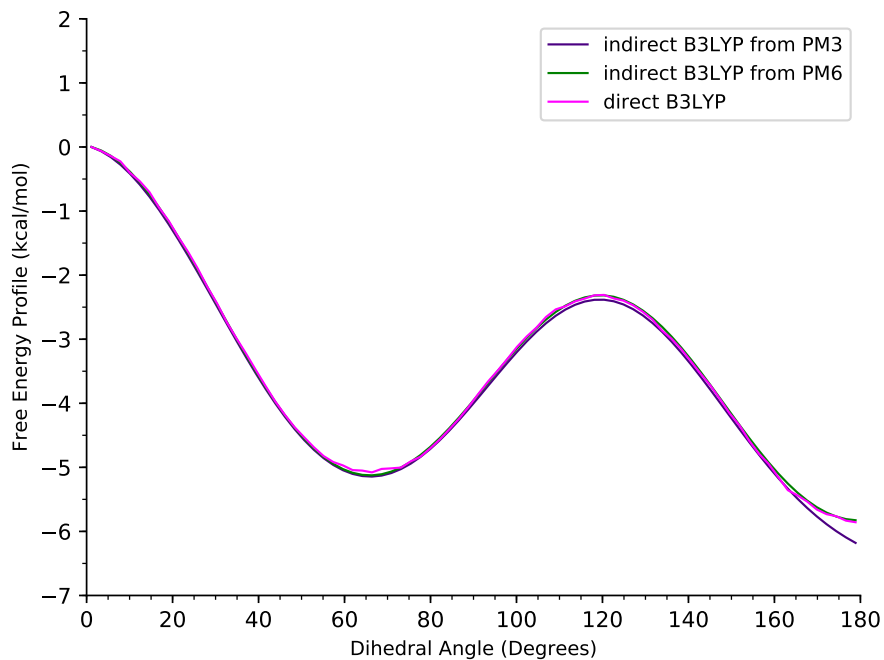


Figure 3: The indirect FE profiles for the main chain dihedral rotation of a butane molecule at B3LYP level calculated by the weighted TP calculations from the PM3 Hamiltonian (indigo) and the PM6 Hamiltonian (green), as well as the direct FE profile at the B3LYP level (magenta).

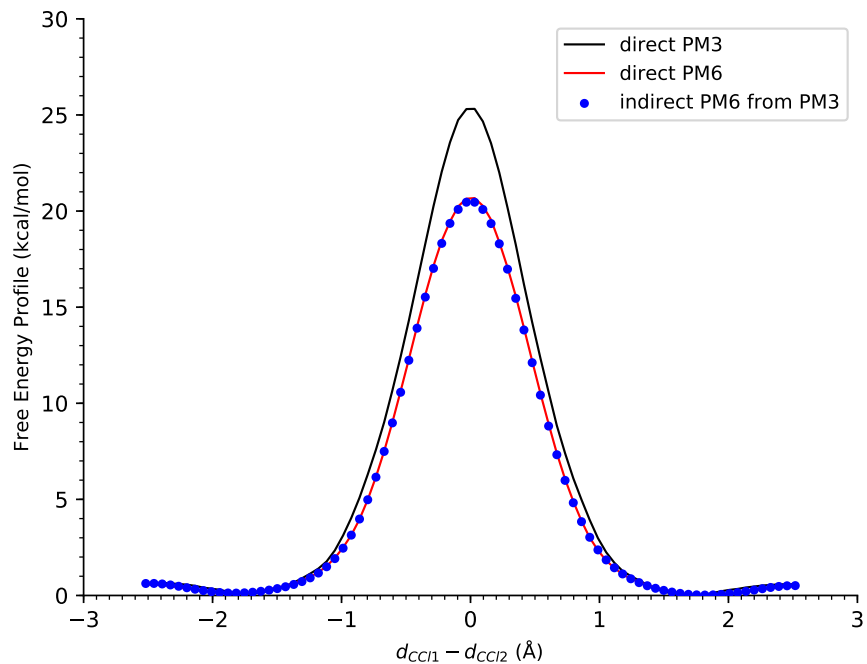


Figure 4: The direct FE profiles for the S_N2 reaction of $CH_3Cl + Cl^- \longrightarrow Cl^- + CH_3Cl$ at the PM3 level (black) and the PM6 level (red), as well as the indirect FE profile at the PM6 level corrected from the PM3 curve (blue dots).

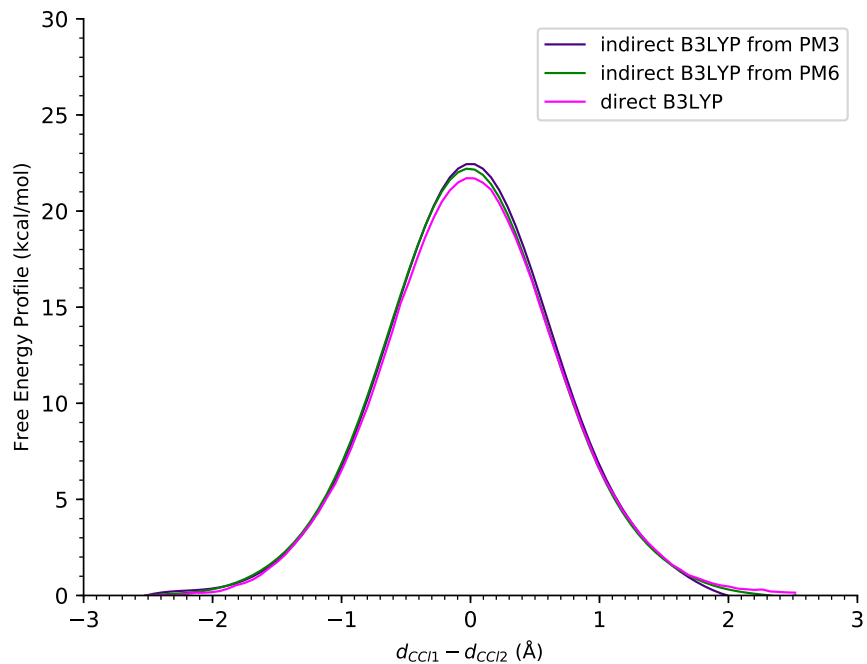


Figure 5: The indirect FE profiles for the S_N2 reaction of $\text{CH}_3\text{Cl} + \text{Cl}^- \longrightarrow \text{Cl}^- + \text{CH}_3\text{Cl}$ at the B3LYP level calculated by the weighted TP calculations from the PM3 Hamiltonian (indigo) and the PM6 Hamiltonian (green), as well as the direct FE profile at the B3LYP level (magenta).

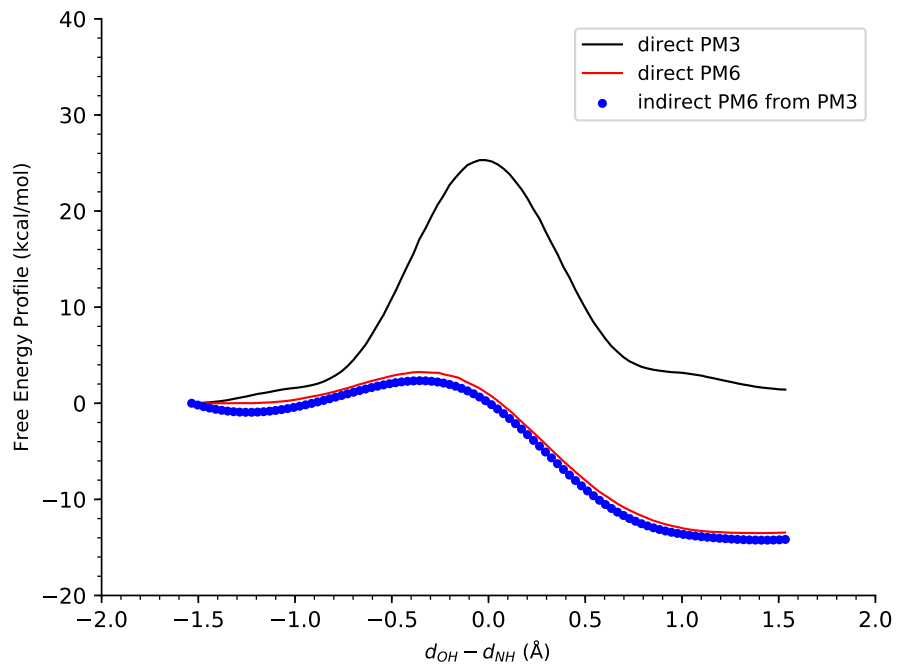


Figure 6: The direct FE profiles for the glycine intramolecular proton transfer reaction at the PM3 level (black) and the PM6 level (red), as well as the indirect FE profile at the PM6 level corrected from the PM3 curve (blue dots).

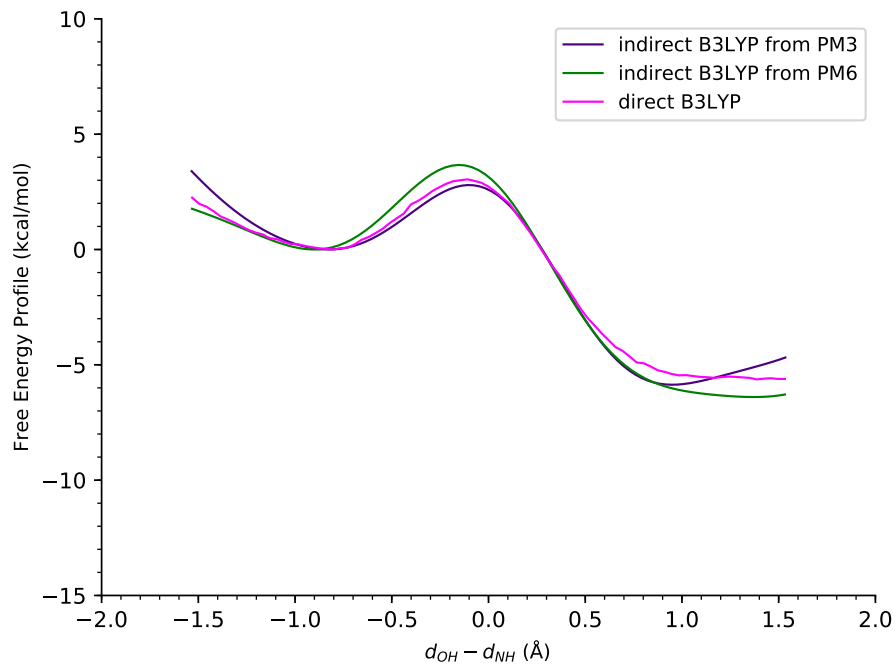


Figure 7: The indirect FE profiles for the glycine intramolecular proton transfer reaction at the B3LYP level calculated by the weighted TP calculations from the PM3 Hamiltonian (indigo) and the PM6 Hamiltonian (green), as well as the direct FE profile at the B3LYP level (magenta).

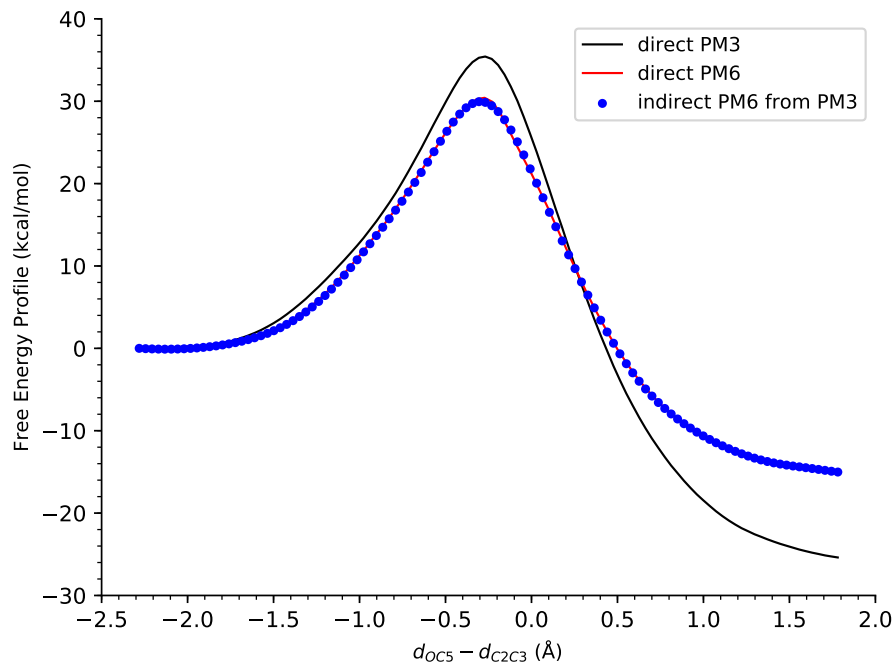


Figure 8: The direct FE profiles for the aliphatic Claisen rearrangement reaction of allyl vinyl ether (AVE) to 4-pentenal at the PM3 level (black) and the PM6 level (red), as well as the indirect FE profile at the PM6 level corrected from the PM3 curve (blue dots).

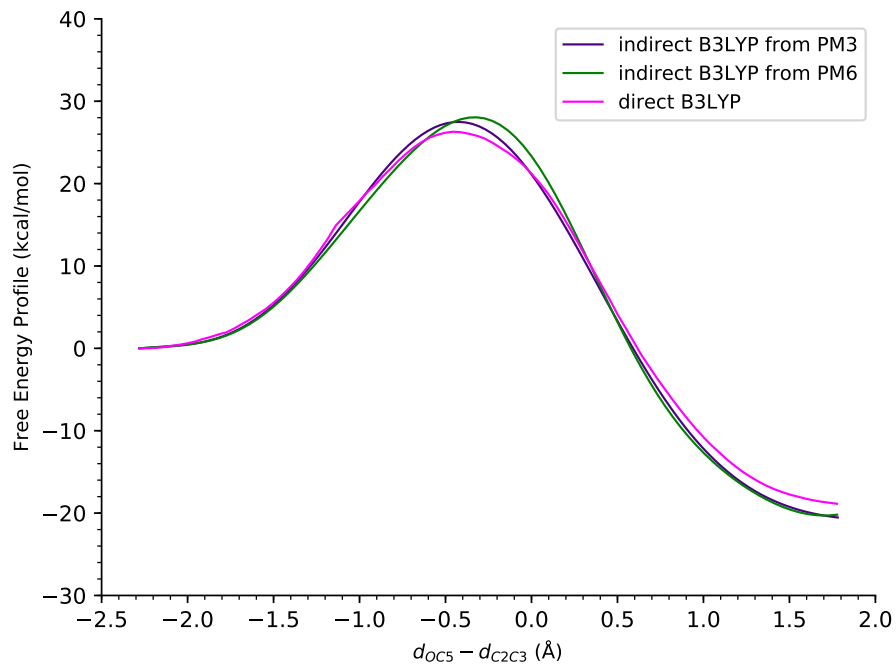


Figure 9: The indirect FE profiles for the aliphatic Claisen rearrangement reaction of allyl vinyl ether (AVE) to 4-pentenal at the B3LYP level calculated by the weighted TP calculations from the PM3 Hamiltonian (indigo) and the PM6 Hamiltonian (green), as well as the direct FE profile at the B3LYP level (magenta).

Table 1: Estimated wall time in a unit of hours for the computations of the QM/MM free energy profiles at the B3LYP/6-31G* level. Assuming one node with 16 cores of Intel Xeon CPU E5-2660 2.20 GHz was used.

Reactions	Wall Time		
	indirect from PM3	indirect from PM6	direct ^a
BT ^b	2205	2212	54900
S _N 2 ^c	2403	3743	55480
PT ^d	2106	1992	91800
CR ^e	3459	3483	101650

^a Using the same number of windows as in the semiempirical simulations, and one 1-ns simulation for each window.

^b The main chain dihedral rotation of a butane molecule.

^c The S_N2 reaction of CH₃Cl + Cl⁻ \longrightarrow Cl⁻ + CH₃Cl.

^d The glycine intramolecular proton transfer reaction.

^e The aliphatic Claisen rearrangement reaction of allyl vinyl ether (AVE) to 4-pentenal.

Supporting Information

**Computation of Free Energy Profile at ab initio
QM/MM Level Made Orders of Magnitude
Faster via the Reference-Potential Approach
Using Weighted Thermodynamics Perturbation**

Pengfei Li,[†] Xiangyu Jia,^{†,§} Yihan Shao,[‡] and Ye Mei^{*,†,¶,‡}

[†]*State Key Laboratory of Precision Spectroscopy, School of Physics and Materials Science,
East China Normal University, Shanghai 200062, China*

[‡]*Department of Chemistry and Biochemistry, University of Oklahoma, Norman OK 73019,
United States of America*

[¶]*NYU-ECNU Center for Computational Chemistry at NYU Shanghai, Shanghai 200062,
China*

[§]*Current address: NYU-ECNU Center for Computational Chemistry at NYU Shanghai,
Shanghai 200062, China*

E-mail: ymei@phy.ecnu.edu.cn

1 Forward and Backward TP are equivalent to BAR for the Weighted Samples from US

Instead of calculating the weights for all the snapshots under the low-level Hamiltonian as in Eq. 9, we can also calculate their weights under the high-level Hamiltonian as

$$\begin{aligned}
 w_H(\mathbf{x}_{i,l}) &= \frac{e^{-\beta[U_H(\mathbf{x}_{i,l}) - f_H]}}{\sum_{k=1}^S N_k e^{-\beta[U_k^{(b)}(\mathbf{x}_{i,l}) - f_k^{(b)}]}}. \\
 &= \frac{e^{-\beta[U_H(\mathbf{x}_{i,l}) - U_L(\mathbf{x}_{i,l})]} e^{\beta f_H}}{\sum_{k=1}^S N_k e^{-\beta[W_k(\mathbf{x}_{i,l}) - f_k^{(b)}]}} ,
 \end{aligned} \tag{S1}$$

where $e^{\beta f_H}$ is an irrelevant constant and will be canceled later in the normalization. With these weights, the free energy difference can be obtained via a TP calculation from the high-level Hamiltonian to the low-level Hamiltonian by

$$\begin{aligned}
 \Delta F(\eta) &= \frac{1}{\beta} \ln \frac{\sum_{i=1}^S \sum_{l=1}^{N_i} w_H(\mathbf{x}_\eta) \delta(\eta_{(i,l)} - \eta) e^{-\beta[U_L(\mathbf{x}_\eta) - U_H(\mathbf{x}_\eta)]}}{\sum_{i=1}^S \sum_{l=1}^{N_i} w_H(\mathbf{x}_\eta) \delta(\eta_{(i,l)} - \eta)} \\
 &= \frac{1}{\beta} \ln \frac{\sum_{i=1}^S \sum_{l=1}^{N_i} w_L(\mathbf{x}_\eta) \delta(\eta_{(i,l)} - \eta)}{\sum_{i=1}^S \sum_{l=1}^{N_i} w_L(\mathbf{x}_\eta) \delta(\eta_{(i,l)} - \eta) e^{-\beta[U_H(\mathbf{x}_{\eta(i,l)}) - U_L(\mathbf{x}_{\eta(i,l)})]}} \\
 &= -\frac{1}{\beta} \ln \frac{\sum_{i=1}^S \sum_{l=1}^{N_i} w_L(\mathbf{x}_{\eta(i,l)}) e^{-\beta[U_H(\mathbf{x}_{\eta(i,l)}) - U_L(\mathbf{x}_{\eta(i,l)})]}}{\sum_{i=1}^S \sum_{l=1}^{N_i} w_L(\mathbf{x}_{\eta(i,l)})},
 \end{aligned} \tag{S2}$$

which is exactly Eq. 10. We can also use Bennett acceptance ratio instead of TP via

$$\Delta F(\eta) = -\beta^{-1} \ln \left[\frac{\langle f(U_H(\mathbf{x}_\eta) - U_L(\mathbf{x}_\eta) - C) \rangle_L \exp(-\beta C)}{\langle f(U_L(\mathbf{x}_\eta) - U_H(\mathbf{x}_\eta) + C) \rangle_H} \right], \tag{S3}$$

where $f(x) = \frac{1}{1+\exp(\beta x)}$ is the Fermi function and $C = \beta^{-1} \ln \frac{Q_L}{Q_H}$ with Q_L and Q_H being the partition function under the low-level and the high-level Hamiltonians, respectively. We can expand the ensemble averages of the Fermi functions as

$$\langle f(U_H(\mathbf{x}_\eta) - U_L(\mathbf{x}_\eta) - C) \rangle_L = \frac{\sum_{i=1}^S \sum_{l=1}^{N_i} w_L(\mathbf{x}_\eta) \delta(\eta_{(i,l)} - \eta) \frac{1}{1+\exp[\beta(U_H(\mathbf{x}_\eta) - U_L(\mathbf{x}_\eta) - C)]}}{\sum_{i=1}^S \sum_{l=1}^{N_i} w_L(\mathbf{x}_\eta) \delta(\eta_{(i,l)} - \eta)} \quad (\text{S4})$$

and

$$\begin{aligned} \langle f(U_L(\mathbf{x}_\eta) - U_H(\mathbf{x}_\eta) + C) \rangle_H &= \frac{\sum_{i=1}^S \sum_{l=1}^{N_i} w_H(\mathbf{x}_\eta) \delta(\eta_{(i,l)} - \eta) \frac{1}{1+\exp[\beta(U_L(\mathbf{x}_\eta) - U_H(\mathbf{x}_\eta) + C)]}}{\sum_{i=1}^S \sum_{l=1}^{N_i} w_H(\mathbf{x}_\eta) \delta(\eta_{(i,l)} - \eta)} \\ &= \frac{\sum_{i=1}^S \sum_{l=1}^{N_i} w_H(\mathbf{x}_\eta) \delta(\eta_{(i,l)} - \eta) \frac{\exp[\beta(U_H(\mathbf{x}_\eta) - U_L(\mathbf{x}_\eta) - C)]}{1+\exp[\beta(U_H(\mathbf{x}_\eta) - U_L(\mathbf{x}_\eta) - C)]}}{\sum_{i=1}^S \sum_{l=1}^{N_i} w_H(\mathbf{x}_\eta) \delta(\eta_{(i,l)} - \eta)} \\ &= \frac{\sum_{i=1}^S \sum_{l=1}^{N_i} w_L(\mathbf{x}_\eta) \delta(\eta_{(i,l)} - \eta) \frac{\exp(-\beta C)}{1+\exp[\beta(U_H(\mathbf{x}_\eta) - U_L(\mathbf{x}_\eta) - C)]}}{\sum_{i=1}^S \sum_{l=1}^{N_i} w_L e^{-\beta[U_H(\mathbf{x}_{i,l}) - f_H]}(\mathbf{x}_\eta) \delta(\eta_{(i,l)} - \eta)} \end{aligned} \quad (\text{S5})$$

Taking Eq. S4 and S5 into Eq. S3, we find

$$\begin{aligned} \Delta F(\eta) &= -\beta^{-1} \ln \left[\frac{\frac{\sum_{i=1}^S \sum_{l=1}^{N_i} w_L(\mathbf{x}_\eta) \delta(\eta_{(i,l)} - \eta) \frac{1}{1+\exp[\beta(U_H(\mathbf{x}_\eta) - U_L(\mathbf{x}_\eta) - C)]}}{\sum_{i=1}^S \sum_{l=1}^{N_i} w_L(\mathbf{x}_\eta) \delta(\eta_{(i,l)} - \eta)}}{\frac{\sum_{i=1}^S \sum_{l=1}^{N_i} w_L(\mathbf{x}_\eta) \delta(\eta_{(i,l)} - \eta) \frac{\exp(-\beta C)}{1+\exp[\beta(U_H(\mathbf{x}_\eta) - U_L(\mathbf{x}_\eta) - C)]}}{\sum_{i=1}^S \sum_{l=1}^{N_i} w_L e^{-\beta[U_H(\mathbf{x}_{i,l}) - f_H]}(\mathbf{x}_\eta) \delta(\eta_{(i,l)} - \eta)}}} \exp(-\beta C) \right] \\ &= -\frac{1}{\beta} \ln \frac{\sum_{i=1}^S \sum_{l=1}^{N_i} w_L(\mathbf{x}_{\eta_{(i,l)}}) e^{-\beta[U_H(\mathbf{x}_{\eta_{(i,l)}}) - U_L(\mathbf{x}_{\eta_{(i,l)}})]}}{\sum_{i=1}^S \sum_{l=1}^{N_i} w_L(\mathbf{x}_{\eta_{(i,l)}})}, \end{aligned} \quad (\text{S6})$$

which is consistent with the TP calculations. These results are not surprising, because these two calculations have the same amount of information as the forward TP shown in the main text.

2 Reliability of the MBAR Analysis of the Trajectories from Umbrella Samplings

The reliabilities of the MBAR calculations are examined by calculating the overlap matrix proposed by Mobley et. al.,¹ which essentially measures the magnitude of the phase space overlap. With the weight of the l th configuration in the i th biased simulation appearing in the t th simulation defined as

$$w_t(\mathbf{x}_{i,l}) = \frac{e^{-\beta[W_t(\mathbf{x}_{i,l}) - f_t^{(b)}]}}{\sum_{k=1}^S N_k e^{-\beta[W_k(\mathbf{x}_{i,l}) - f_k^{(b)}]}}, \quad (\text{S7})$$

the elements of the $S \times S$ overlap matrix are¹

$$\begin{aligned} O_{tt'} &= \sum_{i=1}^S \sum_{l=1}^{N_i} N_i w_t(\mathbf{x}_{i,l}) w_{t'}(\mathbf{x}_{i,l}) \\ &= \sum_{i=1}^S \sum_{l=1}^{N_i} \frac{N_i e^{-\beta[W_t(\mathbf{x}_{i,l}) - f_t^{(b)}]} e^{-\beta[W_{t'}(\mathbf{x}_{i,l}) - f_{t'}^{(b)}]}}{\left\{ \sum_{k=1}^S N_k e^{-\beta[W_k(\mathbf{x}_{i,l}) - f_k^{(b)}]} \right\}^2}. \end{aligned} \quad (\text{S8})$$

Consecutive windows should have substantial overlap with the diagonal and the first off-diagonal elements no smaller than 0.03 as recommended.¹

The US simulations were performed at the PM3 and PM6 and B3LYP levels, from which the FE profiles were calculated by the MBAR method. In order to assess whether the phase space overlap between each pair of the neighboring windows was sufficient, the overlap matrices were calculated for these trajectories. As shown in Fig. S1 for the dihedral rotation of butane, all elements in the diagonal and the first off-diagonals of all matrices are larger than 0.22. As shown in Fig. S5 for the S_N2 reaction, all elements in the diagonal and the first off-diagonals of all matrices are larger than 0.1. As shown in Fig. S9 for the proton transfer in glycine, all elements in the diagonal and the first off-diagonals of all matrices are all larger than 0.07. As shown in Fig. S13, all elements in the diagonal and the first off-diagonals of all

matrices are no smaller than 0.09. All of them are larger than the lower-limit 0.03, indicating that the phase space overlap is sufficient for the subsequent MBAR analysis. Therefore, the SQM and QM/MM FE profiles calculated by the MBAR method are statistically reliable.

References

- (1) Klimovich, P. V.; Shirts, M. R.; Mobley, D. L. Guidelines for the Analysis of Free Energy Calculations. *J. Comput. Aid. Mol. Des.* **2015**, *29*, 397–411.

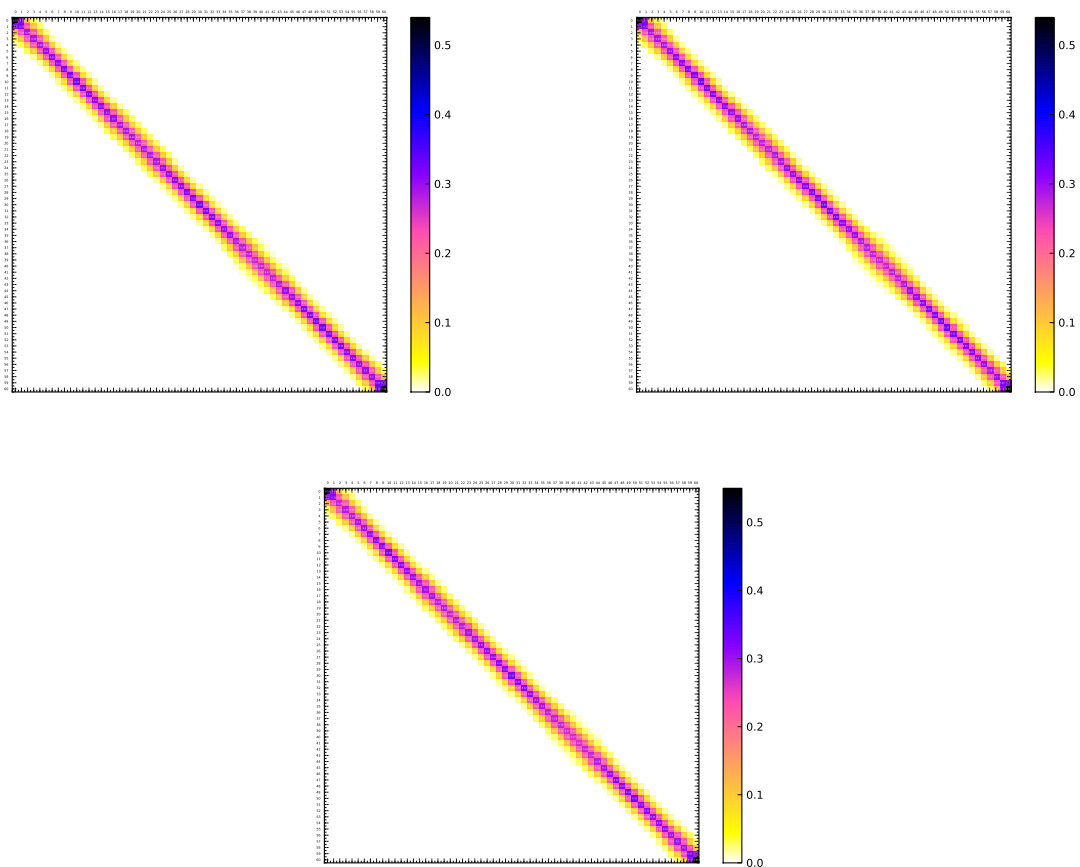


Figure S1: The overlap matrices for the US simulations at the PM3 level (upper left) and the PM6 level (upper right) and the B3LYP level (bottom) for the main chain dihedral rotation of a butane molecule.

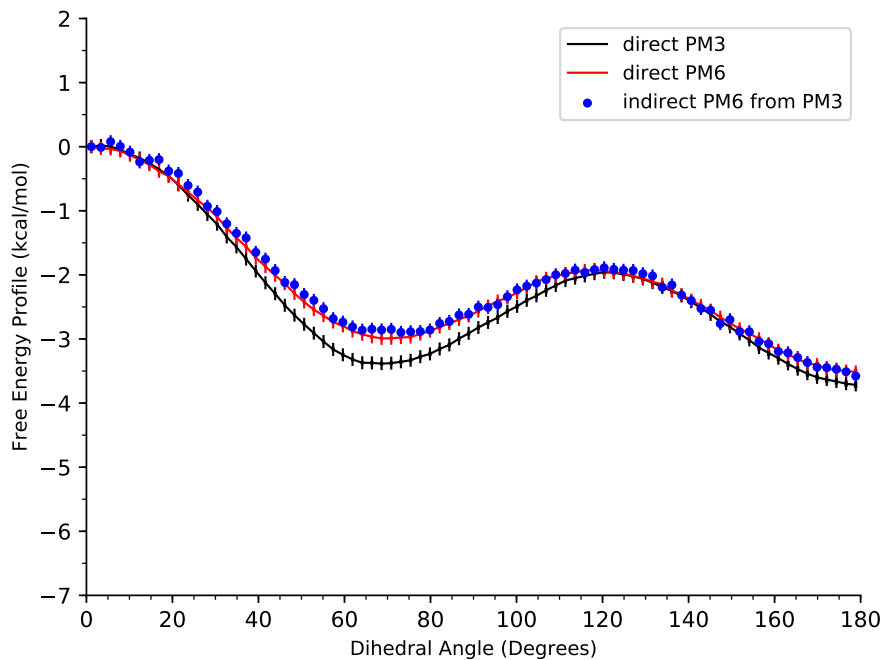


Figure S2: The direct FE profiles as well as their standard deviations for the main chain dihedral rotation of a butane molecule at the PM3 level (black) and the PM6 level (red), as well as the indirect FE profile at the PM6 level corrected from the PM3 curve (blue dots).

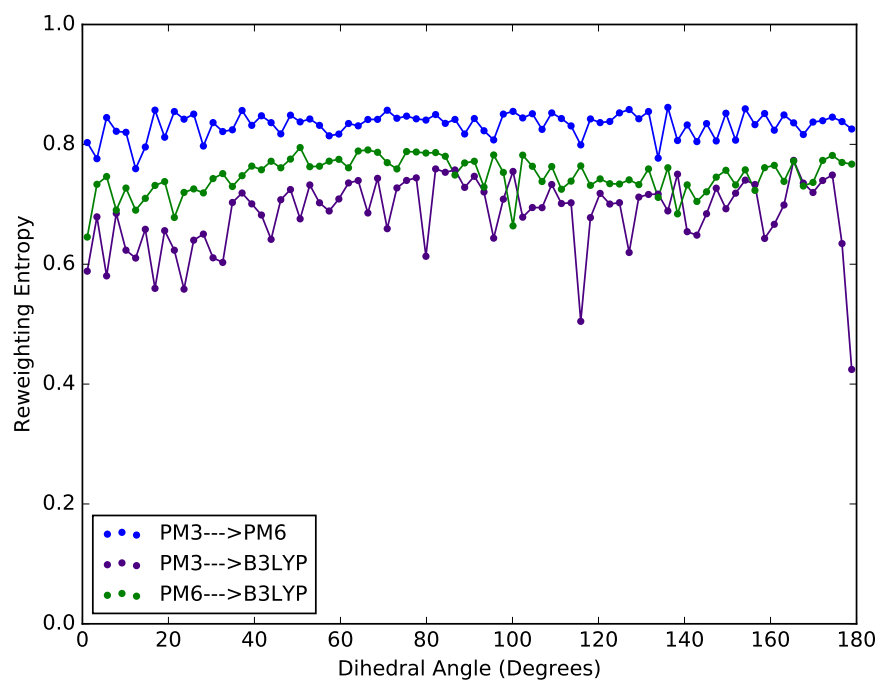


Figure S3: The reweighting entropies in the weighted TP calculations for the main chain dihedral rotation of a butane molecule.

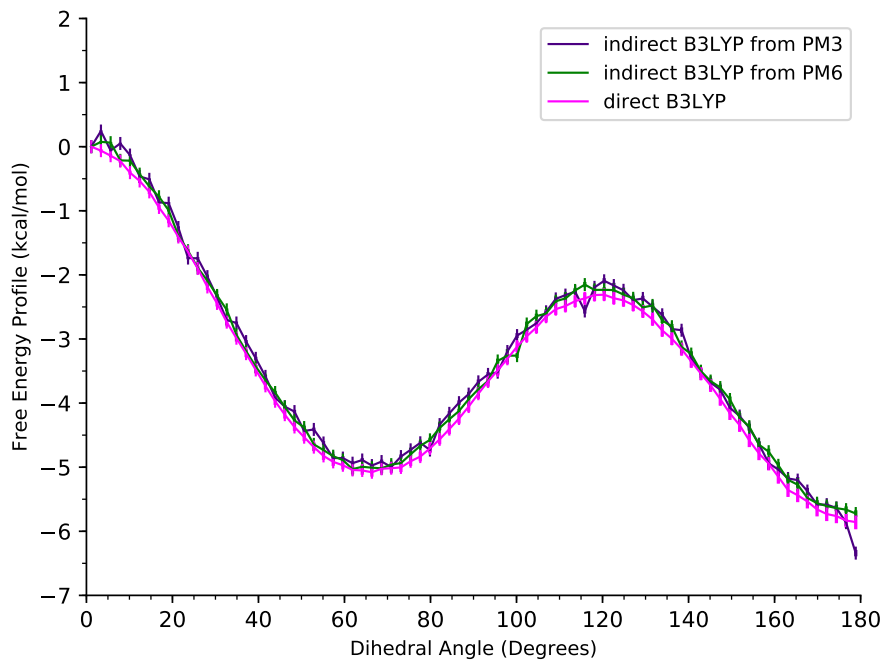


Figure S4: The indirect FE profiles as well as their standard deviations for the main chain dihedral rotation of a butane molecule at the B3LYP level calculated by the weighted TP calculations from the PM3 Hamiltonian (indigo) and the PM6 Hamiltonian (green), as well as the direct FE profile at the B3LYP level (magenta).

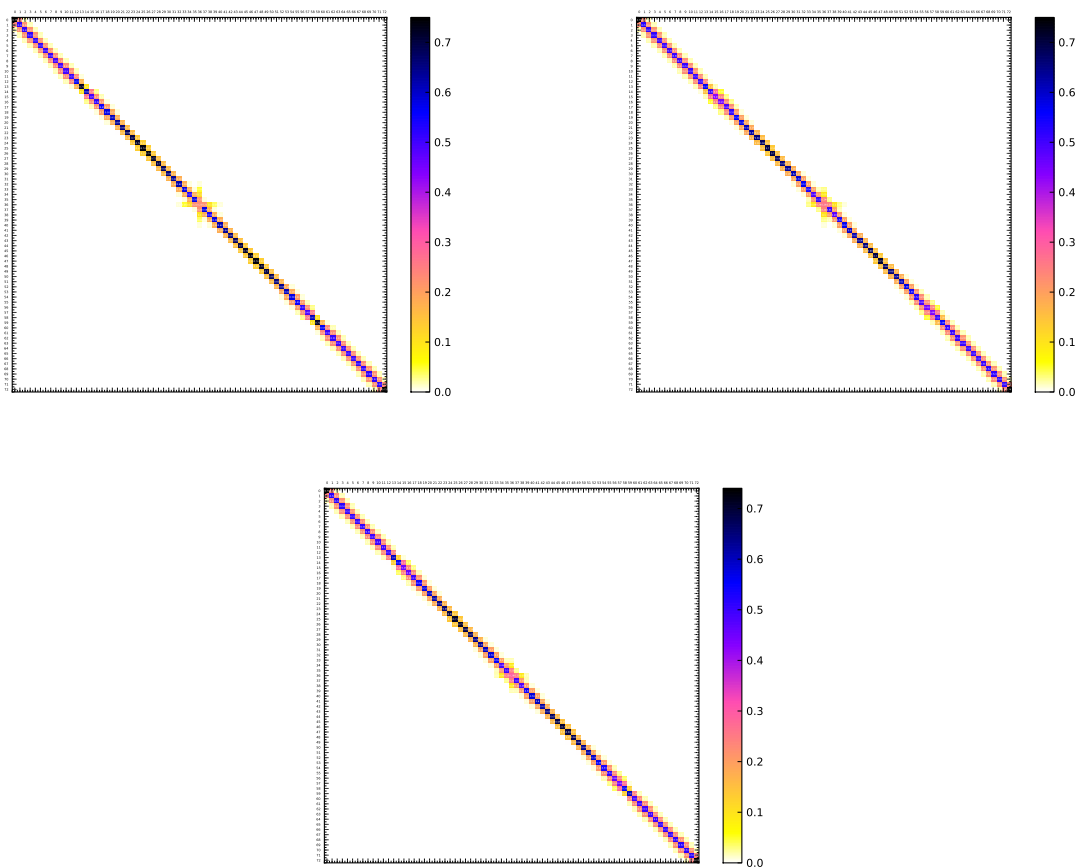


Figure S5: The overlap matrices for the US simulations at the PM3 level (upper left) and the PM6 level (upper right) and the B3LYP level (bottom) for the S_N2 reaction of $\text{CH}_3\text{Cl} + \text{Cl}^- \longrightarrow \text{Cl}^- + \text{CH}_3\text{Cl}$.

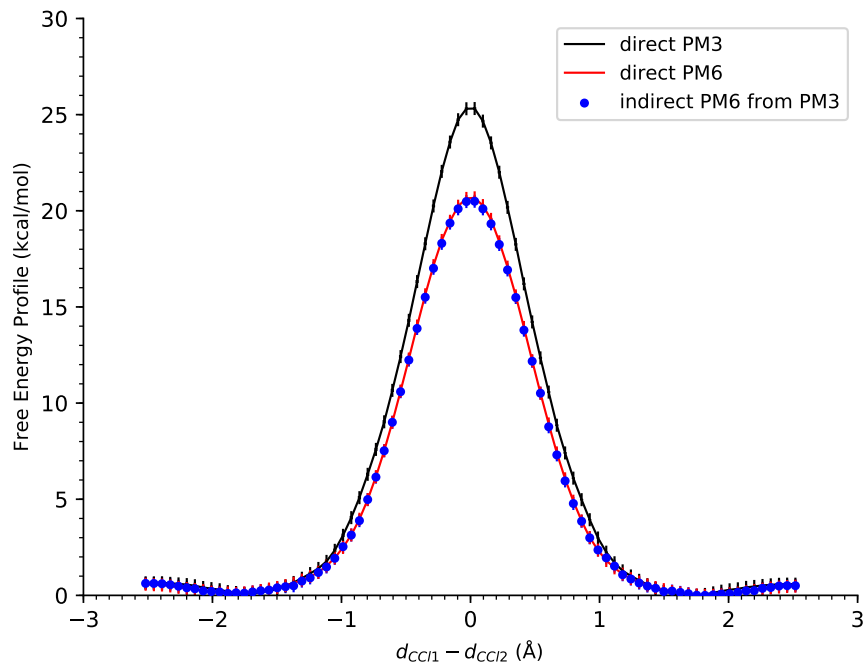


Figure S6: The direct FE profiles as well as their standard deviations for the S_N2 reaction of $\text{CH}_3\text{Cl} + \text{Cl}^- \longrightarrow \text{Cl}^- + \text{CH}_3\text{Cl}$ at the PM3 level (black) and the PM6 level (red), as well as the indirect FE profile at the PM6 level corrected from the PM3 curve (blue dots).

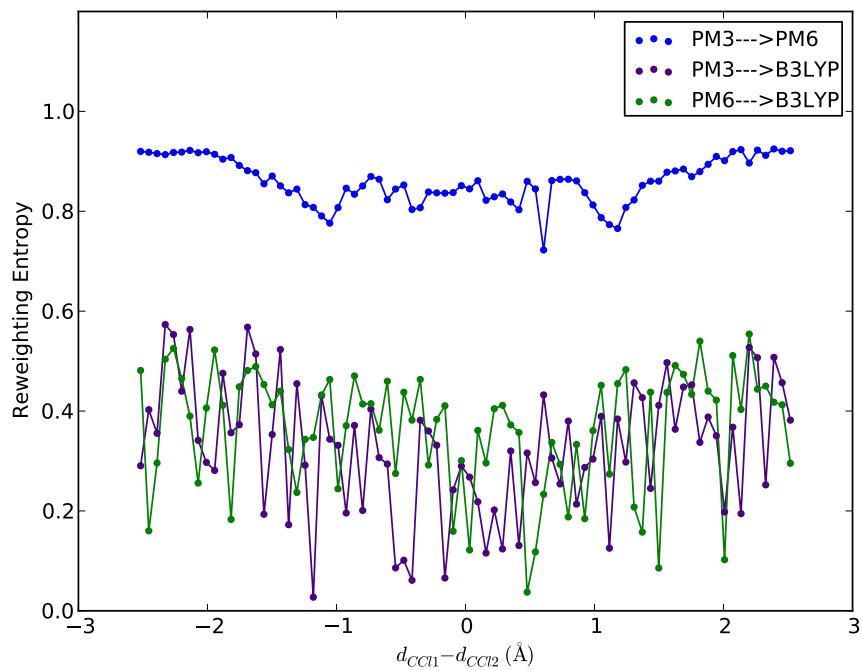


Figure S7: The reweighting entropies in the weighted TP calculations for the S_N2 reaction of $\text{CH}_3\text{Cl} + \text{Cl}^- \longrightarrow \text{Cl}^- + \text{CH}_3\text{Cl}$.

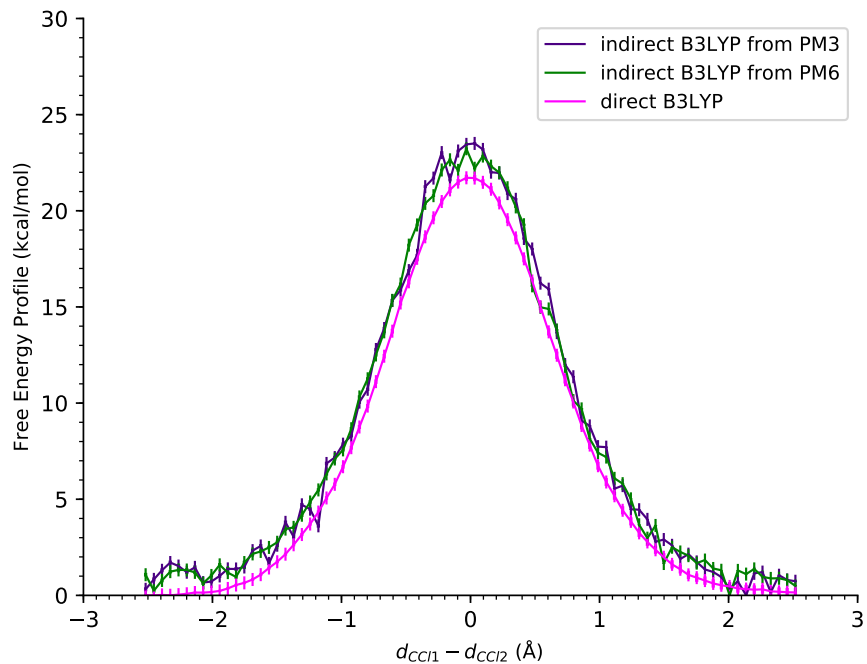


Figure S8: The indirect FE profiles as well as their standard deviations for the S_N2 reaction of $\text{CH}_3\text{Cl} + \text{Cl}^- \longrightarrow \text{Cl}^- + \text{CH}_3\text{Cl}$ at B3LYP level calculated by the weighted TP calculations from the PM3 Hamiltonian (indigo) and the PM6 Hamiltonian (green), as well as the direct FE profile at the B3LYP level (magenta).

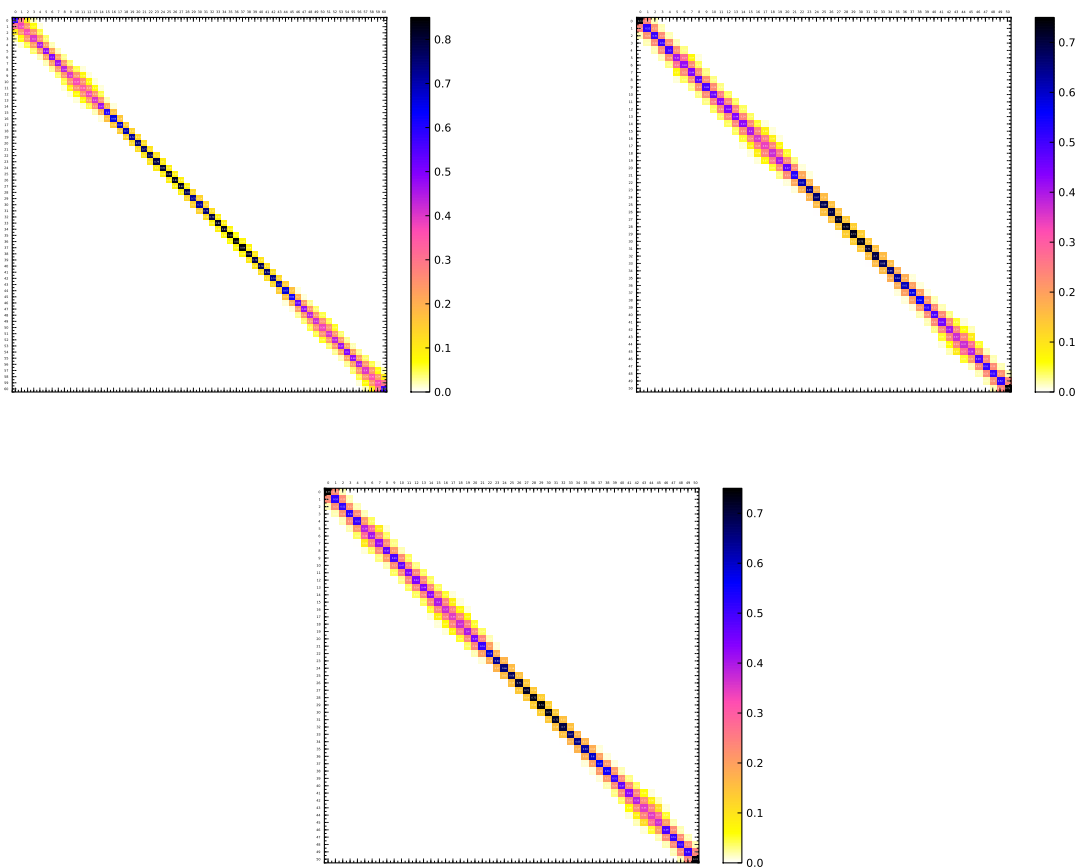


Figure S9: The overlap matrices for the US simulations at the PM3 level (upper left) and the PM6 level (upper right) and the B3LYP level (bottom) for the glycine intramolecular proton transfer reaction.

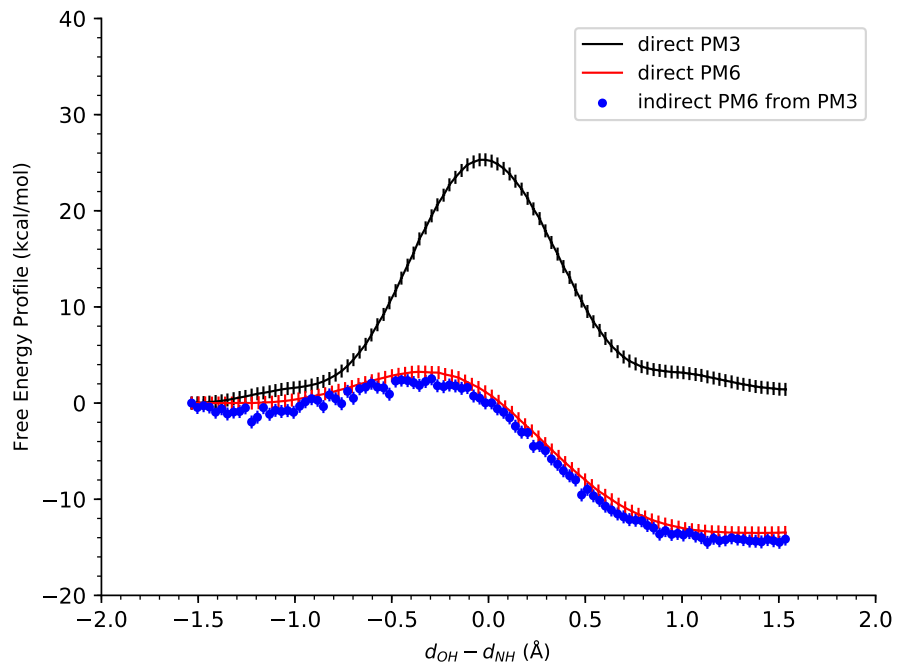


Figure S10: The direct FE profiles as well as their standard deviations for the glycine intramolecular proton transfer reaction at the PM3 level (black) and the PM6 level (red), as well as the indirect FE profile at the PM6 level corrected from the PM3 curve (blue dots).

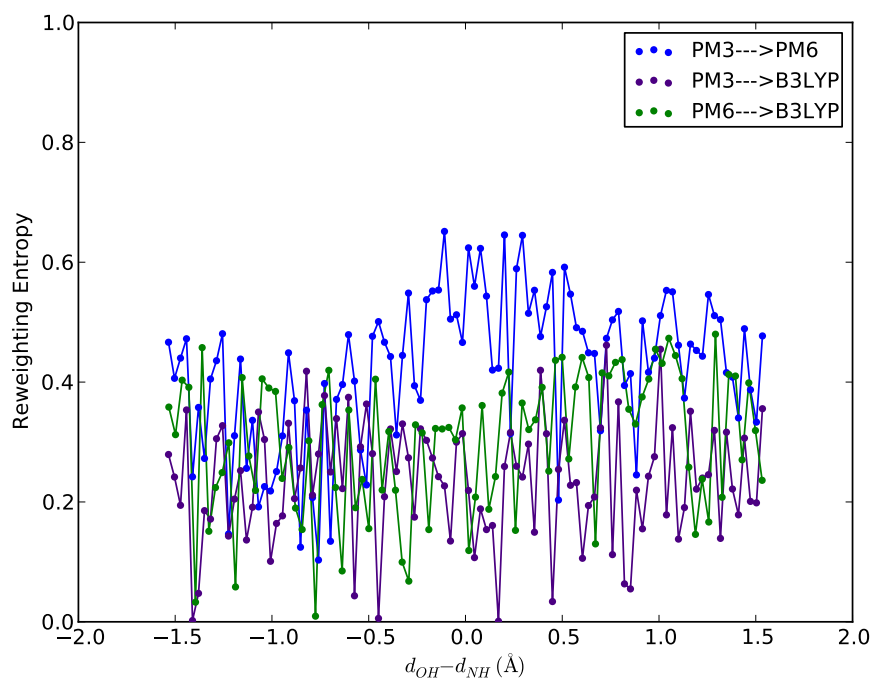


Figure S11: The reweighting entropies in the weighted TP calculations for the glycine intramolecular proton transfer reaction.

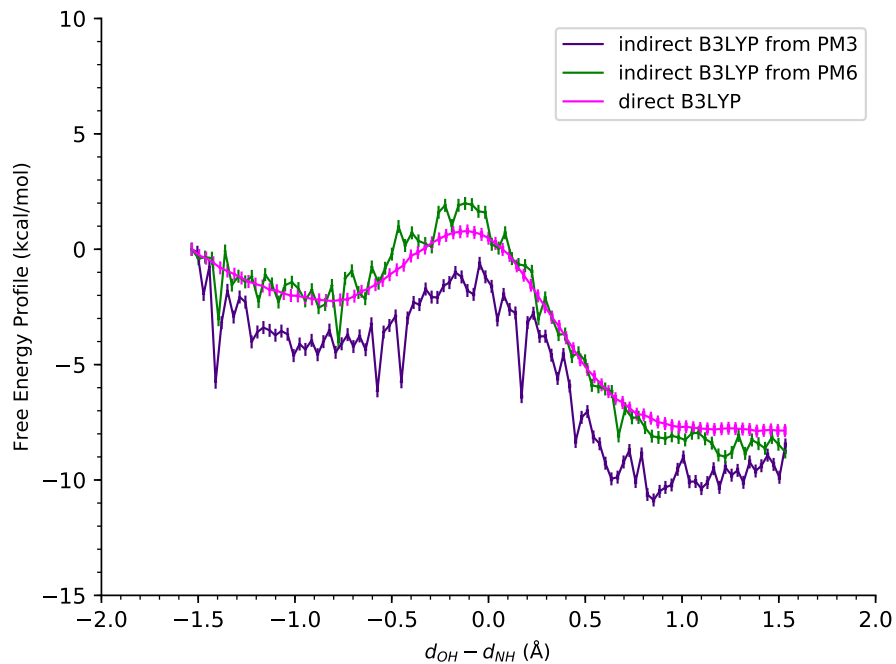


Figure S12: The indirect FE profiles as well as their standard deviations for the glycine intramolecular proton transfer reaction at B3LYP level calculated by the weighted TP calculations from the PM3 Hamiltonian (indigo) and the PM6 Hamiltonian (green), as well as the direct FE profile at the B3LYP level (magenta).

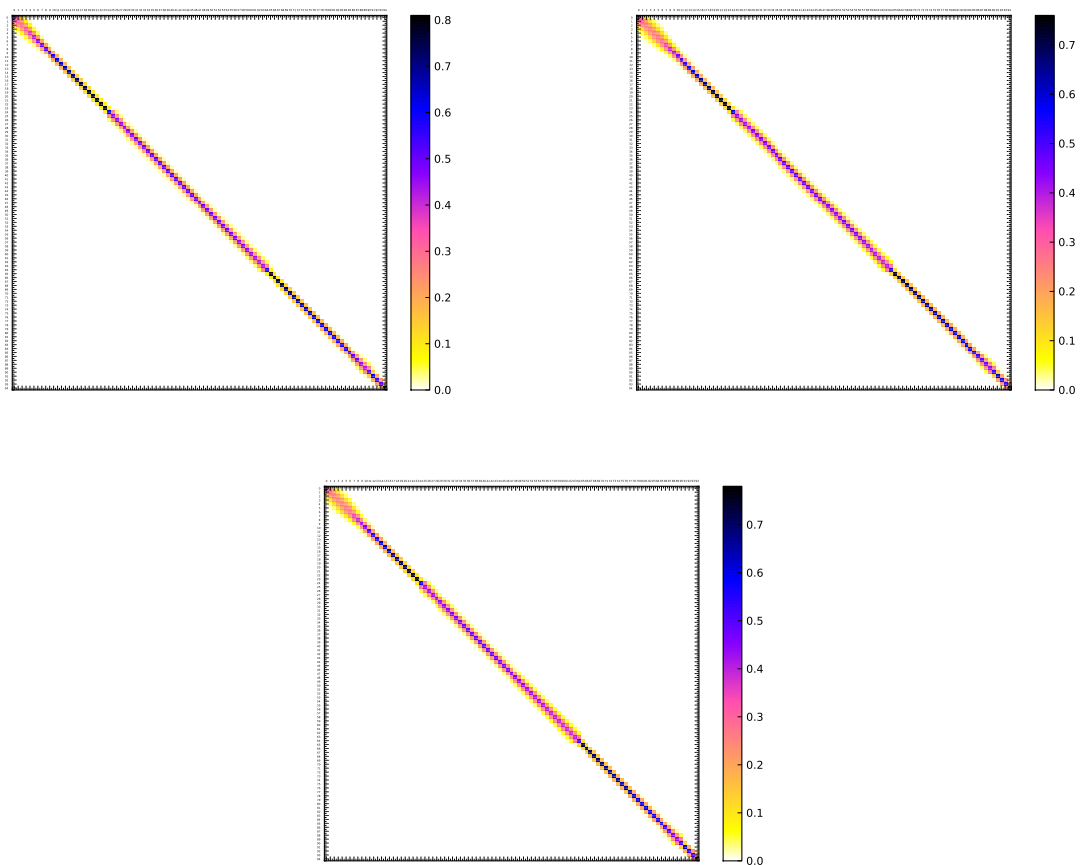


Figure S13: The overlap matrices for the US simulations at the PM3 level (upper left) and the PM6 level (upper right) and the B3LYP level (bottom) for the aliphatic Claisen rearrangement reaction of allyl vinyl ether (AVE) to 4-pentenal.

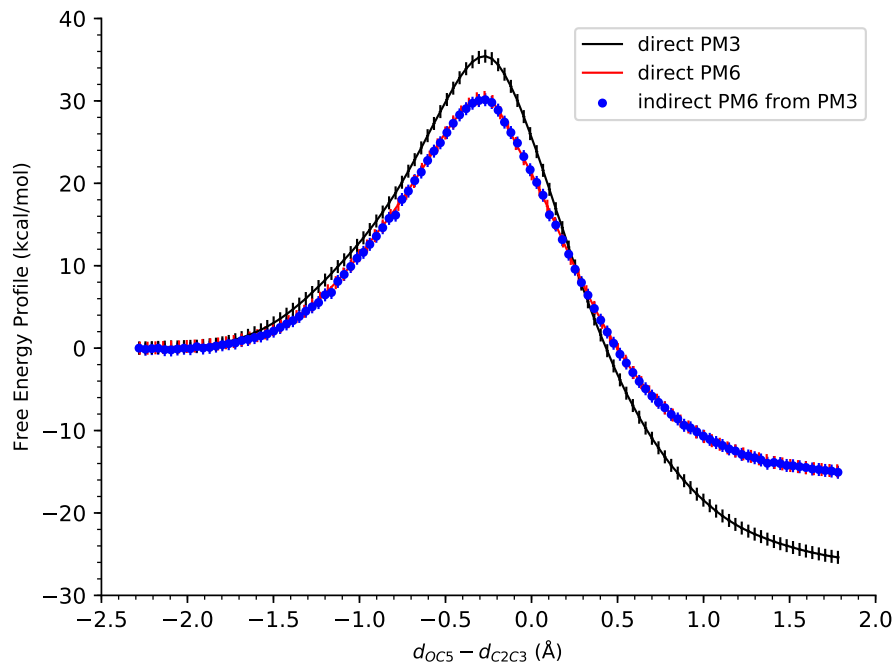


Figure S14: The direct FE profiles as well as their standard deviations for the aliphatic Claisen rearrangement reaction of allyl vinyl ether (AVE) to 4-pentenal at the PM3 level (black) and the PM6 level (red), as well as the indirect FE profile at the PM6 level corrected from the PM3 curve (blue dots).

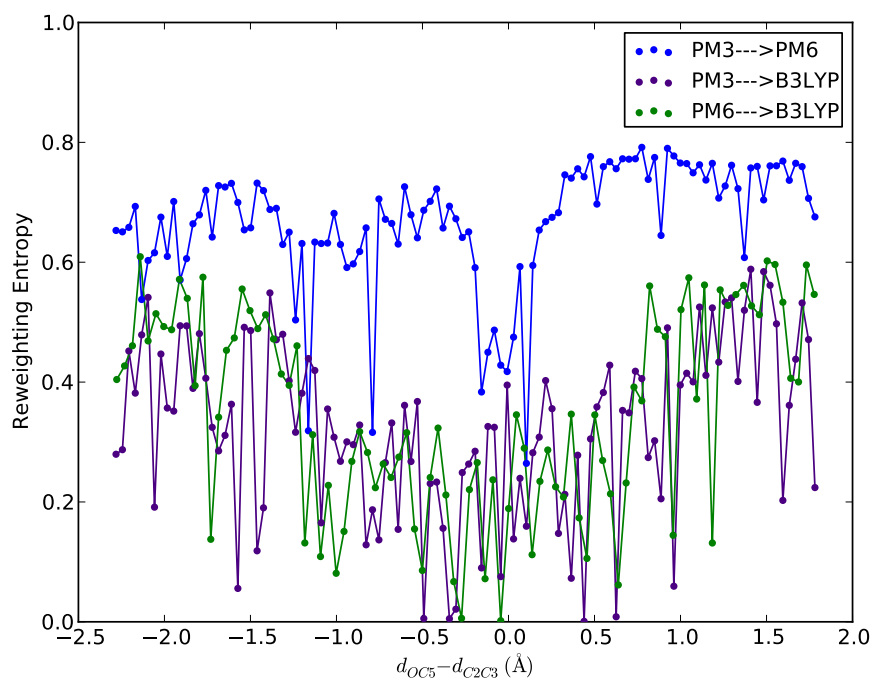


Figure S15: The reweighting entropies in the weighted TP calculations for the aliphatic Claisen rearrangement reaction of allyl vinyl ether (AVE) to 4-pentenal.

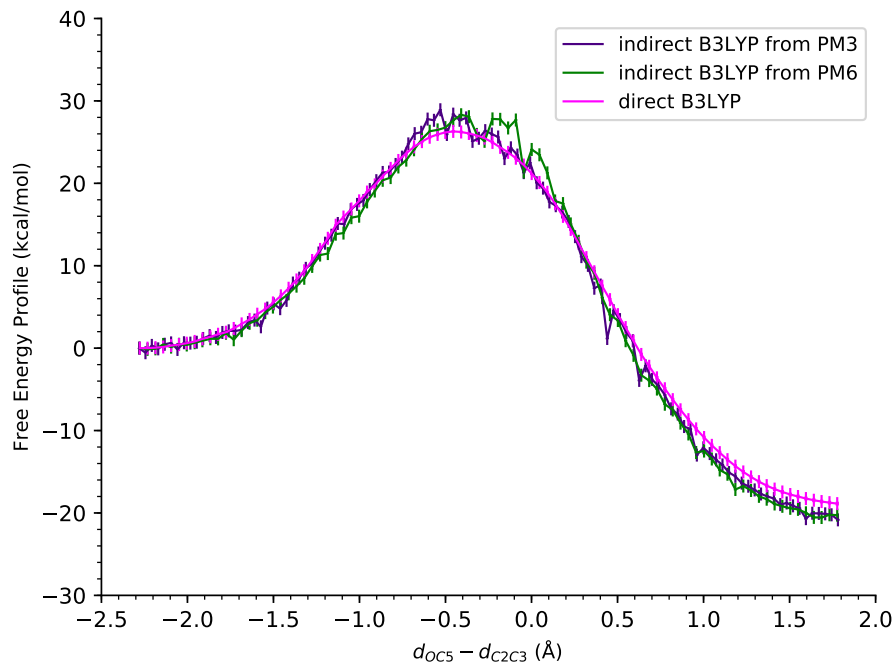


Figure S16: The indirect FE profiles as well as their standard deviations for the aliphatic Claisen rearrangement reaction of allyl vinyl ether (AVE) to 4-pentenal at the B3LYP level calculated by the weighting TP calculations from the PM3 Hamiltonian (indigo) and the PM6 Hamiltonian (green), as well as the direct FE profile at the B3LYP level (magenta).

Graphical TOC Entry

